

1 Spatial influence of fault-related stress perturbations in northern
2 Switzerland

3 Lalit Sai Aditya Reddy Velagala^{1,4}, Oliver Heidbach^{1,2}, Moritz Ziegler^{1,3}, Karsten Reiter⁴, Mojtaba Rajabi⁵, Andreas Henk⁴, Silvio
4 B. Giger⁶, Tobias Hergert⁷.

5 1 GFZ Helmholtz Centre for Geosciences, Telegrafenberg, 14473 Potsdam, Germany.

6 2 Institute for Applied Geosciences, Technische Universität Berlin, 10587 Berlin, Germany.

7 3 Professorship of Geothermal Technologies, Technical University Munich, 80333 Munich, Germany.

8 4 Institute of Applied Geosciences, Technische Universität Darmstadt, 64287 Darmstadt, Germany.

9 5 School of the Environment, The University of Queensland, QLD, 4072, Australia.

10 6 National Cooperative for the Disposal of Radioactive Waste, 5430 Wettingen, Switzerland.

11 7 Institute of Applied Geosciences, Karlsruhe Institute of Technology, 76131 Karlsruhe, Germany.

12 **Abstract**

13 The spatial influence of faults on the crustal stress field is a topic of ongoing debate. While faults are often known
14 to perturb the stress field at a meter scale, their lateral influence over a few hundred meters to several kilometers
15 remains poorly understood. To address this knowledge gap, we use a 3D geomechanical numerical model based
16 on 3D seismic data from northern Switzerland. The model is calibrated with 45 horizontal stress magnitude data
17 obtained from micro-hydraulic fracturing (MHF) and sleeve re-opening (SR) tests conducted in two boreholes in
18 the Zürich Nordost (ZNO) siting region, northern Switzerland. This model with seven faults implemented as
19 contact surfaces serves as the reference model in our study. The reference model is systematically compared to
20 three fault-agnostic models, which share identical rock properties, model dimensions, and calibration data with
21 the reference model, but differ in their element resolution and mechanical properties' assignment procedure.
22 Results show that at distances <1 km from faults, differences in maximum horizontal stress orientation between
23 models range from 3° – 6° , and horizontal stress magnitude differences are approximately 1–2 MPa. Beyond 1 km,
24 these differences reduce to $<1.5^\circ$ and <0.5 MPa, respectively. These differences are significantly smaller than the
25 calibration data uncertainties at ZNO, which average to ± 0.7 MPa and ± 3.5 MPa for the minimum horizontal and
26 maximum horizontal stress magnitude, respectively, and $\pm 11^\circ$ for the maximum horizontal stress orientation. An
27 important implication of our results is that, under the specific geological, mechanical, and stress conditions
28 observed at the ZNO siting region, explicit representation of faults may not be necessary in geomechanical
29 models predicting the stress state of rock volumes located a kilometer or more from active faults. This
30 simplification substantially reduced our model setup time from 2 months to 2 days, without compromising the
31 reliability of stress field predictions.

32 **Short summary**

33 We assess the fault impact on the stress field in northern Switzerland using 3D geomechanical models, calibrated
34 with stress data. We see that faults affect the stresses only locally, with negligible impact beyond 1 km,
35 suggesting that faults may not be necessary in reservoir-scale models predicting stresses of undisturbed rock
36 volumes, such as for a geological repository. Omitting them can substantially reduce model set-up time and
37 computational cost without compromising prediction reliability.

38 **1. Introduction**

39 Characterizing the crustal stress field is essential for understanding both global and local tectonic deformation
40 processes. On a large scale, it provides insights into plate tectonics (Richardson et al., 1979; Cloetingh and Wortel,
41 1985; Rajabi et al., 2017b) and earthquake mechanics (Sibson, 1992; Sibson et al., 2011; Brodsky et al., 2020),
42 while on a local scale, it plays a critical role in the safe planning of many subsurface applications, including oil
43 and gas exploration and storage (Berard et al., 2008; Zoback, 2009; Fischer and Henk, 2013), geothermal
44 exploration (Catalli et al., 2013; Schoenball et al., 2014; Azzola et al., 2019) and deep geological repositories for
45 nuclear waste (Long and Ewing, 2004; Gens et al., 2009; Jo et al., 2019). The present day stress state also
46 significantly impacts wellbore stability and trajectory optimization, reducing risks and improving drilling
47 operations (Kingsborough et al., 1991; Henk, 2005; Rajabi et al., 2016). Moreover, knowledge of the regional and

48 local stress field aids in assessing seismic hazards and understanding the potential generation or reactivation of
49 faults (Zakharova and Goldberg, 2014; Seithel et al., 2019; Vadacca et al., 2021).

50 The stress state at a point is described by the Cauchy stress tensor, a symmetric second-order tensor with six
51 independent components. This tensor can be transformed into a principal stress system, where only three
52 mutually perpendicular normal stresses, known as the principal stresses (S_1 = maximum principal stress; S_2 =
53 intermediate principal stress, and S_3 = minimum principal stress), remain, and the shear stresses are zero. In
54 reservoir geomechanics, where the target area is the upper crust, it is typically assumed that the principal
55 stresses are the vertical stress (S_v), the maximum horizontal stress ($S_{H\max}$), and the minimum horizontal stress
56 ($S_{H\min}$). Based on this, the reduced stress tensor is defined by the magnitudes of S_v , $S_{H\max}$, and $S_{H\min}$, and the
57 orientation of $S_{H\max}$ (Jaeger et al., 2007; Zoback, 2009).

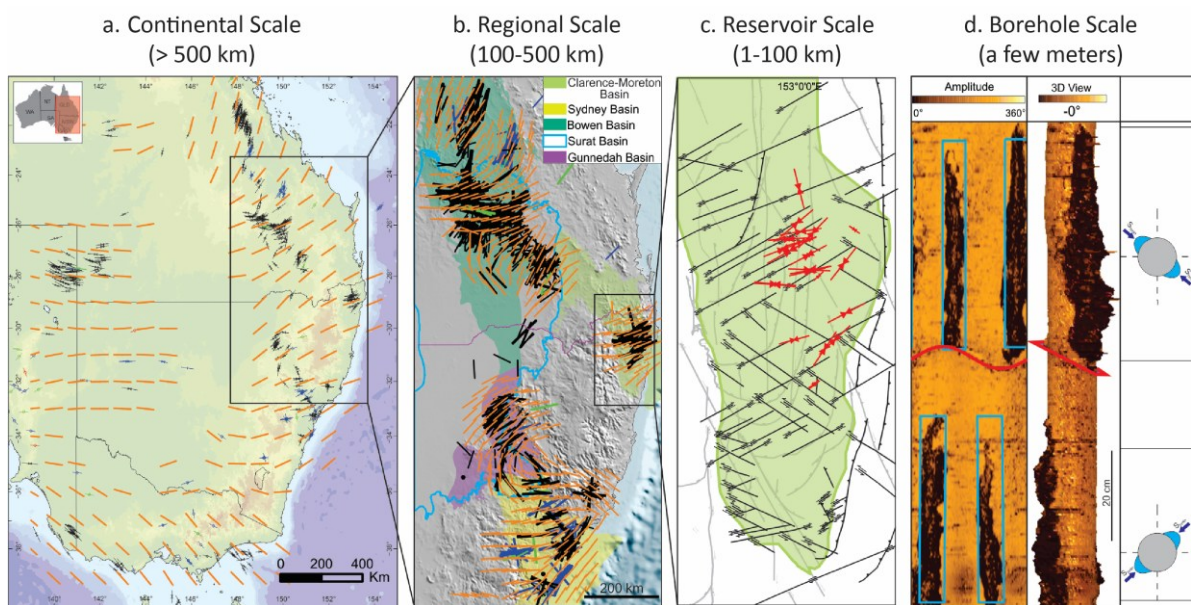
58 The $S_{H\max}$ orientation is the most widely available, systematically documented, and freely accessible characteristic
59 of the reduced stress tensor, compiled in a publicly available database of the World Stress Map project (Heidbach
60 et al., 2018; Heidbach et al., 2025a). Analyzing the patterns of the $S_{H\max}$ orientation shows consistent trends over
61 hundreds of kilometers in intra-continental areas, primarily driven by first-order plate tectonic forces and
62 second-order buoyancy forces (Zoback et al., 1989; Zoback, 1992; Rajabi et al., 2017b; Heidbach et al., 2018). At
63 the same time, in some regions, significant rotations exceeding 30° are observed on spatial scales ranging from
64 a few tens to a few hundreds of kilometers. It is hypothesized that these variations in $S_{H\max}$ orientations, among
65 other reasons, arise from faults (Zoback et al., 1987; Yale, 2003; Heidbach et al., 2007; Tingay et al., 2009; Rajabi
66 et al., 2017b).

67 A common approach to understanding the fault impact on the stress field is to visually interpret laterally
68 scattered $S_{H\max}$ orientation data. This often leads to attributing the observed variability in $S_{H\max}$ orientation to the
69 faults present within their respective study areas (Yale et al., 1994; Bell, 1996b; Yale, 2003; Aleksandrowski et
70 al., 1992). While these studies are often convincing, they face two key issues: First, even in areas with relatively
71 high data coverage, such as northern Switzerland (Heidbach et al., 2025a; Heidbach et al., 2025b) and the
72 northern Bowen Basin (Rajabi et al., 2024; Heidbach et al., 2025a), the data density is fairly low, with, on average,
73 one data record per 138 km² lateral spatial distance, and one data record per 80 km² lateral spatial distance,
74 respectively. Second, individual $S_{H\max}$ orientations have an average standard deviation of ±15° (A-Quality) to ±25°
75 (C-Quality), as defined in the World Stress Map (Heidbach et al., 2025a). Together, these issues do not allow for
76 attributing with confidence small rotations in the $S_{H\max}$ orientations to the faults, especially at spatial scales of
77 0.1–10 km.

78 Notable studies from regions with a comprehensive $S_{H\max}$ orientation dataset show that large-scale faulting does
79 not necessarily result in abrupt rotations in the $S_{H\max}$ orientation over continental (>500 km) and regional scales
80 (100–500 km). For instance, in eastern Australia, the $S_{H\max}$ orientation rotates smoothly, by up to 50° over less
81 than 100 km despite varying dip and strikes of the major fault systems, from northern Bowen Basin to southern
82 Bowen and Surat basins (Brooke-Barnett et al., 2015; Tavener et al., 2017; Rajabi et al., 2024) (Fig. 1a-b).
83 However, in the adjacent Clarence-Moreton Basin, rotation of $S_{H\max}$ orientations is prominent and abrupt when
84 viewed in conjunction with the faults (Rajabi et al., 2015; Rajabi et al., 2017b; Rajabi et al., 2017c) (Fig. 1a-b).
85 Comparable conflicting trends have been reported in other studies as well (Bell and Gough, 1979; Gough and
86 Bell, 1982; Bell and Grasby, 2012), suggesting that the influence of fault systems on the rotation of $S_{H\max}$
87 orientation at continental and regional scales is not straightforward, and often not resolvable without ambiguity.

88 At the borehole scale, distinct variations in $S_{H\max}$ orientation have been observed vertically on a spatial scale of a
89 few meters. For instance, Fig. 1d shows an image log of a borehole from the Clarence-Moreton Basin, where the
90 $S_{H\max}$ orientation abruptly changes by 90° when the borehole intersects a fault. This is also observed in the San
91 Andreas Fault Observatory Drilling Borehole, where borehole breakouts (BO) and drilling-induced tensile
92 fractures (DITF) indicate a change in $S_{H\max}$ orientation from 25° ± 10° at 1000–1500 m to 70° ± 14° at 2050–2200
93 m (Chéry et al., 2004; Hickman and Zoback, 2004; Boness and Zoback, 2006; Zoback et al., 2011). Also, in the KTB
94 drilling program, $S_{H\max}$ orientation along the borehole remained consistent with the regional tectonic-induced
95 patterns except at a depth of 7200 m, where a major fault zone caused a localized reorientation by about 60°,
96 confined to only a few meters above and below the fault (Brudy et al., 1993; Barton and Zoback, 1994; Brudy et
97 al., 1997).

98 However, borehole-scale studies are generally conducted in vertical wells and do not capture the potential lateral
 99 variations in stress caused by faults. Therefore, it remains unclear whether these localized findings can directly
 100 be extrapolated to explain stress field variations at larger spatial scales away from the fault zone. This leads to a
 101 significant knowledge gap regarding fault's influence on stress field variations at the reservoir scale (Fig. 1c), a
 102 scale particularly important for many subsurface applications. The only viable approach for predicting the
 103 variations in the stress field at this scale is geomechanical numerical modelling. Over the past few decades, 2D
 104 and 3D geomechanical numerical models have been developed for this purpose (Henk, 2009, 2020; Treffeisen
 105 and Henk, 2020). These can broadly be grouped into three categories: 1) site-specific models without fault
 106 representation (Lecampion and Lei, 2010; Rajabi et al., 2017c; Ahlers et al., 2021), 2) site-specific models that
 107 include faults but are not explicitly focused on assessing influence of faults on the predicted stress (Reiter and
 108 Heidbach, 2014; Hergert et al., 2015; Bérard and Desroches, 2021) and 3) generic models that explicitly
 109 investigates the impact of faults (Homberg et al., 1997; Su and Stephansson, 1999; Reiter et al., 2024; Ziegler et
 110 al., 2024). While models without faults are understandably not suitable for evaluating fault-related stress
 111 perturbations, the latter two categories often have limited or no access to reliable *in situ* stress magnitude data.
 112 This hinders their ability to reliably represent fault-related stress variations in real-world scenarios.



113 Figure 1: $S_{H\max}$ orientation stress map from eastern Australia at a) Continental scale; b) Regional scale; c) Reservoir scale, and
 114 d) Borehole scale. On continental and regional scales, visual observations suggest that faults may have differing influences,
 115 as seen in the uniform stress orientation (orange lines) across eastern Australia despite the presence of faults. However, on
 116 a borehole scale, faults can cause local perturbations, evident in the shift of borehole breakout orientations (blue box), which
 117 reflect stress variations across the fault (red line) (Image adopted from Rajabi et al. (2017c)).

118 In our study, we use 45 reliable and robust stress magnitudes data records, obtained from two deep boreholes,
 119 Trüllikon (TRU1-1) and Marthalen (MAR1-1), using microhydraulic fracturing (MHF) and dry sleeve re-opening
 120 (SR) test (Desroches et al., 2021a; Desroches et al., 2021b; Desroches et al., 2023) to calibrate 3D geomechanical
 121 numerical models of the Zürich Nordost (ZNO) siting region, northern Switzerland (Fig. 2). The data records were
 122 collected during a comprehensive 3D seismic and drilling campaign to support site selection for a deep geological
 123 repository (DGR) of radioactive waste (Nagra, 2024c, a). The stress magnitudes presented in this study are the
 124 total stresses, and any reference to the stress magnitudes must be taken as such. Four variants of the 3D
 125 geomechanical numerical model of the siting region, each with lateral dimensions of 14.7 km \times 14.8 km, and a
 126 vertical depth of 2.5 km (below sea level; b.s.l), are used within this study. All models use identical mechanical
 127 properties and the same representation of geomechanically relevant subsurface units. One of the models
 128 includes seven contact surfaces with an assigned friction coefficient representing faults, and serves as the
 129 reference model (REF model) (Nagra, 2024d, c), while the other three models are fault-agnostic, i.e., faults are
 130 excluded from the model. By systematically comparing the predicted stress fields across all the models, we
 131 illustrate the observed perturbations in the stress field with respect to the reference model and quantify the
 132 spatial extent of the stress perturbations caused by faults.

134 2. 3D geomechanical numerical model with fault representation

135 2.1 Geological background and model geometry

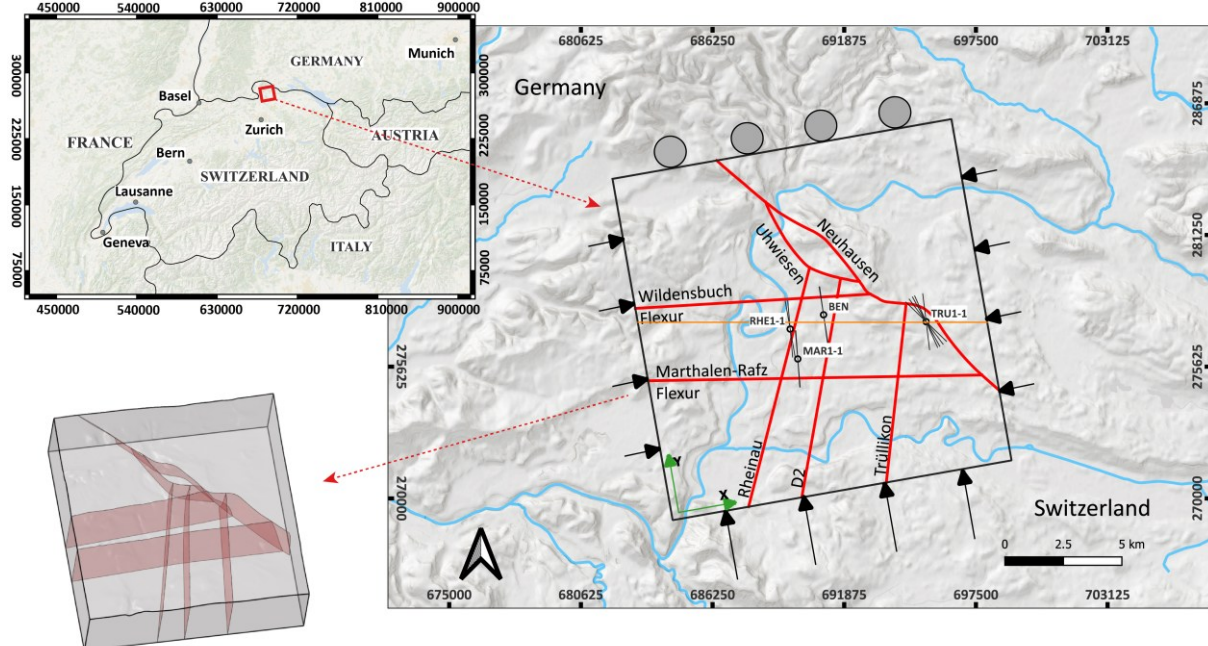
136 The ZNO study region is located in the northern Alpine Foreland of northern Switzerland, approximately 30 km
137 NNE of Zurich (Fig. 2). It is close to the SW of Germany, where pre-Mesozoic basement rocks locally outcrop
138 (Nagra, 1984, 2002a). The geological evolution of this region was influenced by the development of a WSW–ENE
139 striking Permo-Carboniferous basin (Gorin et al., 1993; Mccann et al., 2006; Nagra, 2014), formed in response to
140 the Variscan orogeny and subsequent post-orogenic transtensional processes (Nagra, 1991; Marchant et al.,
141 2005).

142 During the Mesozoic, a sequence of sedimentary successions was deposited on top of the Variscan basement.
143 This depositional process was prominent, especially from the Early to Middle Jurassic due to a combination of
144 regional tectonic subsidence and sea level change (Coward and Dietrich, 1989; Nagra, 2024c). The sedimentary
145 rocks were originally deposited directly on the ocean floor as a result of the landmass corresponding to the
146 present day northern Switzerland being submerged in a broad and shallow epicontinental marine setting (Jordan,
147 2008; Reisdorf et al., 2011). The Opalinus Clay formation, deposited during the Jurassic Period of the Mesozoic
148 Era, is of particular importance as it has been selected as the host rock for Switzerland's DGR. Factors contributing
149 to the effectiveness of Opalinus Clay as a long-term geological barrier are its favorable mineralogy and associated
150 low permeability, and good sorption and self-sealing properties (Nagra, 2001, 2002b, 2008).

151 At the late Cretaceous and onset of the Cenozoic, the Alpine orogeny, formed by the collision of Adriatic and
152 Eurasian tectonic plates, led to a significant tectonic activity in the European northern Alpine Foreland (Illies,
153 1972; Schmid et al., 1996; Schmid et al., 1997; Cloetingh et al., 2006). This resulted in the formation of basement-
154 rooted, NNE-striking normal faults, forming the Upper Rhine Valley in combination with the uplift of the Black
155 Forest and Vosges Mountain Massifs. The formation of the flexural Molasse Basin during the Late Oligocene to
156 Early Miocene is a result of downbending of the European plate, in response to the orogenic loading of the Alps,
157 and caused a gentle dip from north to south in the Mesozoic strata (Sinclair and Allen, 1992; Kempf and Adrian,
158 2004; Sommaruga et al., 2012). In our study region, the Mesozoic strata gently dips SSE (Fig. 3). In the Late
159 Miocene, continued Alpine deformation propagated into the northern Foreland, resulting in the formation of the
160 Jura Mountains and their associated fold-and-thrust belt, primarily further to the west, and reactivating the pre-
161 existing basement structures (Diebold and Noack, 1997; Burkhard and Sommaruga, 1998; Laubscher, 2010).
162 These tectonic processes, along with the glacial-interglacial cycles during the Pleistocene (Fiebig and Preusser,
163 2008; Preusser et al., 2011), have established the present day geological and stratigraphic setting in the region.

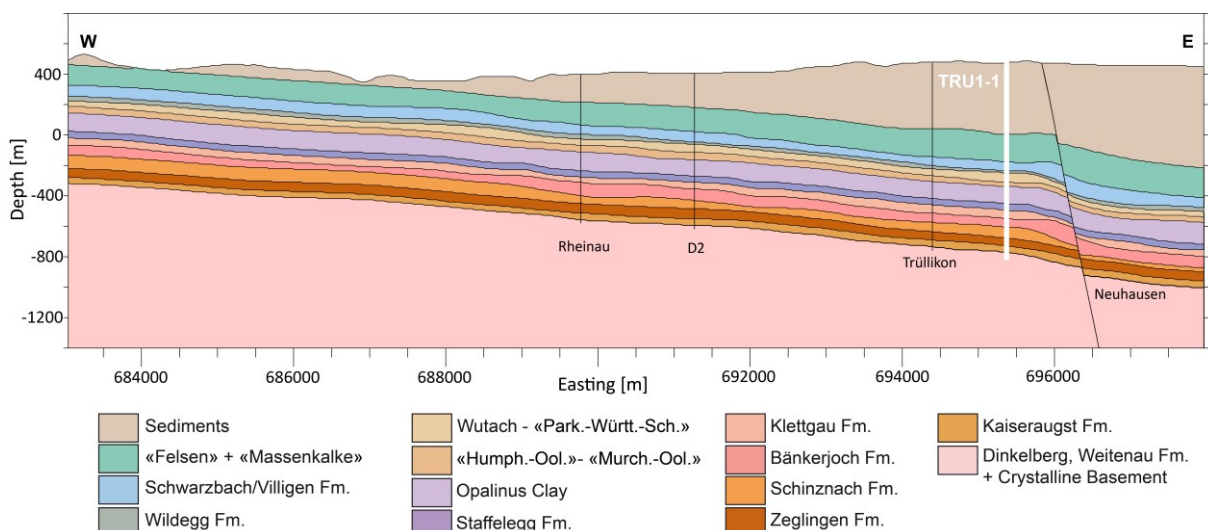
164 The reference model (REF model) is rectangular, spanning 14.7 km E-W × 14.8 km N-S laterally, and extending to
165 a depth of 2.5 km below sea level (b.s.l.). The upper boundary is defined by the local topography. In the siting
166 region, $S_{H\max}$ orientation is $170^\circ \pm 11^\circ$ according to the BO and DITF observations from the boreholes, in
167 agreement with the regional trend (Nagra, 2013; Heidbach et al., 2025b). To align the model geometry with the
168 $S_{H\max}$ orientation, the entire model domain is rotated by 10° counterclockwise from geographic north, such that
169 its sides are parallel and perpendicular to the mean $S_{H\max}$ orientation (Fig. 2).

170 The present day geomechanically relevant layers were constructed using SKUA-GOCAD v19 software. Successive
171 lithologies with comparable mechanical properties were combined (Table 1), eventually leading to 14
172 geomechanically different units in the REF model (Fig. 3). A total of seven faults and flexures, named Neuhausen,
173 Uhwiesen, Wildensbuch, Marthalen-Rafz Flexure, Rheinau, D2, and Trüllikon, were implemented in the model
174 (Fig. 2). These structures are modeled as contact surfaces, weakly interpreted from the regional 3D seismic
175 sections, and are highly simplified for ease of implementation in the model. Here, simplification means merging
176 much smaller segments interpreted on 3D seismics into larger, continuous fault planes to represent what is, in
177 reality, a volumetric fault zone structure (Nagra, 2024a) (Fig. 2, 3).



180
 181 Figure 2: Geographical location and the model boundaries of the ZNO siting region. The red lines within the model extents
 182 represent the surface trace of the faults and flexures, interpreted from the seismic sections of the siting region and
 183 extrapolated to the surface. The location of the boreholes Trüllikon (TRU1-1), Benken (BEN), Marthalen (MAR1-1), and
 184 Rheinau (RHE1-1) is shown, along with the $S_{H\max}$ orientation data records from each borehole (black lines with the centre at
 185 the boreholes). The light brown line is the surface trace of a W-E cross-section, along which all the results in our study are
 186 plotted. The black arrows on the sides of the model are the displacement boundary conditions. The grey circles in the north
 187 of the model indicate that the displacements are constrained perpendicular to this boundary. The coordinate reference
 188 system used is CH1903. The insert at the bottom left is the 3D view of the faults (light-red) within the model geometry (grey
 189 box).

190 Both Neuhausen and Uhwiesen faults dip at 60° toward the northeast, while the others are vertical. Neuhausen
 191 is the only fault that has a stratigraphic offset, with a vertical displacement of approximately 50 m at the base of
 192 the Mesozoic units that decreases towards the surface (Nagra, 2002a, 2008, 2024d). The Marthalen-Rafz Flexur
 193 and Wildensbuch Flexur are monoclines that dominate the overlying Mesozoic strata in the siting region through
 194 a step-like bending rather than a discrete break in an otherwise dipping strata (Madritsch et al., 2024; Nagra,
 195 2024c). Other than the Neuhausen fault, the remaining faults and flexures show no clear displacement but are
 196 included in the model as they represent the first-order geological structures of the ZNO siting region.



199 Figure 3: W-E cross-section of the geomechanical units passing through the Trüllikon borehole (Bold white line, TRU1-1) and
 200 a constant northing = 277548 m within the REF model domain. The depth is referenced to the sea level. Vertical exaggeration

201 by a factor of 2.5 is applied to enhance the visibility of thin layers, such as the Wildegg Formation. The respective mechanical
202 properties are shown in Table 1. Only depths down to -1400 m (b.s.l) are shown for clarity, although the REF model extends
203 to -2500 m (b.s.l). The coordinate reference system used is CH1903.

204 2.2 Reference model (REF model) setup

205 2.2.1 Model assumptions

206 The primary objective of the REF model is to reliably predict the present day stress state within the ZNO siting
207 region. To achieve this, two key simplifying assumptions are made. First, transient effects such as time-
208 dependent tectonic deformation or human-induced changes are neglected while considering only the stress
209 contributions from the gravitational and tectonic forces. Since the model focuses on static stress field prediction,
210 the rock volume is assumed not to undergo any transient deformation. Second, linear isotropic elasticity is
211 assumed in the geomechanical units within the rock volume. This assumption simplifies the material parameters
212 needed to explain the behavior of the rock under stress to just the Young's modulus which characterizes the
213 elastic stiffness of the rock (E), Poisson's ratio which describes the lateral strain response (ν), and density (ρ) of
214 each geomechanical unit. Throughout this work, we will refer to Young's modulus as stiffness and the contrast
215 in Young's modulus as stiffness contrast. The equilibrium condition between the gravitational and the tectonic
216 forces is governed by a second-order partial differential equation (PDE), with displacement as the field variable
217 (Jaeger et al., 2007). Since this PDE cannot be solved analytically, a numerical solution is needed. Therefore, we
218 use the Finite Element Method (FEM). FEM allows the use of unstructured meshes to represent the model
219 volume, which is particularly useful when modeling complex geological features and variations in material
220 properties (Mao, 2005; Henk, 2009).

221 Although several studies have shown that the stress state can be dominated by inelastic deformations once the
222 elastic limits of the geomechanical units are exceeded (Smart et al., 2012; Pijnenburg et al., 2019; Yan et al.,
223 2025), linear elasticity remains an appropriate first-order approximation for predicting the present day stress
224 state in the ZNO siting region. This assumption is supported by several geological factors (Nagra, 2024d, c). The
225 tectonic strain rates in northern Switzerland are extremely low, in the order of 1-3 m/Myr/km, and the region is
226 tectonically stable, with no significant deformation observed since the Miocene. More importantly, the observed
227 differential stresses (S_1 - S_3) within the geomechanical units range between 0.5–13 MPa, which are significantly
228 lower than their measured uniaxial compressive strength limits of 33–180 MPa. Because the differential stresses
229 in the geomechanical units are far below their peak strength, plastic deformation is not expected under the
230 current stress state.

231 2.2.2 Model discretization

232 The model setup follows a standard series of steps, previously used in other regional geomechanical studies
233 (Buchmann and Connolly, 2007; Reiter and Heidbach, 2014; Hergert et al., 2015; Ziegler et al., 2016; Rajabi et al.,
234 2017a). The model volume is discretized into 3D elements, collectively referred to as a mesh. The 3D element
235 resolution plays a significant role in capturing predicted stress variations, where smaller elements capture a
236 higher spatial resolution but at increased computational cost (Ahlers et al., 2021; Ahlers et al., 2022). To ensure
237 a reasonably accurate representation of each geomechanical unit, a minimum of three finite elements is used in
238 the vertical direction. Accordingly, the top 13 geomechanical units, which are relatively thin (Fig. 3), are
239 discretized with smaller element sizes vertically, whereas the deeper and thicker Basement unit is represented
240 with larger element sizes in the vertical direction. A total of 1,923,139 tetrahedral and hexahedral finite elements
241 are used, providing a high-resolution representation of the geomechanical units, with model resolutions varying
242 from 100-150 m laterally and 5-20 m vertically. We use first-order elements in this study, and the discretization
243 is done using Altair HyperMesh 2021 software package.

244 2.2.3 Mechanical rock properties and fault properties.

245 Geological units with similar mechanical properties are grouped into the same geomechanical unit for simplicity.
246 Each element in the mesh is assigned mechanical properties based on the corresponding geomechanical unit.

247 The mechanical properties E [GPa], v [-], and ρ [kg/m³] used in the models are derived from petrophysical logs
 248 and from uniaxial and triaxial compression tests performed on the core samples obtained from the TRU1-1 and
 249 MAR1-1 boreholes (Nagra, 2024c, b). From the distribution of values for each geomechanical unit, the median
 250 values (P50) are used for the model, summarized in Table 1. Geological faults are implemented as contact
 251 surfaces that can slip under mechanical loading as a structural response to stress conditions, depending on their
 252 frictional properties. In the REF model, contact surfaces are assigned a friction coefficient of 1 and a zero
 253 cohesion, values chosen to best represent the fault properties in the region (Nagra, 2024c).

254 Table 1: Different geological formations with respective mechanical properties. The abbreviations are used solely to indicate
 255 the respective formations in the figures of this paper. Throughout the rest of this paper, the respective units can also be
 256 matched with the corresponding colors shown in Fig. 3 and with the abbreviations given here. Detailed information on the
 257 lithology is given in (Nagra, 2024c, b).

System	Group	Formation	Lithology	Abbreviation	ρ [kg/m ³]	v [-]	E [GPa]
Quaternary, Paleogene, and Neogene		Cenozoic Sediments	Sandstone (calc.)	CeSe	2350	0.30	15
Jurassic	Malm	«Felsenkalke» + «Massenkalk»	Limestone	MaFeMa	2685	0.18	31
		Schwarzbach-Villigen Fm.	Limestone (argill.)	MaScVi	2685	0.20	40
		Wildegg Fm.	Limestone	MaWi	2610	0.26	18
	Dogger	Wutach Fm.	Calc. marl	DoWuVaPa	2530	0.32	13
		Variansmergel Fm.	Silty marl				
		«Parkinsoni-Wütembergica-Sch. »	Silty marl				
		«Humphriesoolith Fm. »	Silty marl	DoHuWeMu	2540	0.28	14
		Wedelsandstein Fm.	Silty marl				
		«Murchisonae-Oolith Fm.»	Silty marl				
		Opalinus Clay Fm.	Silty claystone	DoOp	2520	0.37	11
	Lias	Staffelegg Fm.	Argill. marl	LiSt	2540	0.26	18
Triassic	Keuper	Klettgau Fm.	Dol. Marl	KeKl	2570	0.23	17
		Bänkerjoch Fm.	Anhydrite	KeBä	2700	0.22	23
	Muschelkalk	Schinznach Fm.	Dolostone, Limestone	MuSc	2710	0.24	32
		Zeglingen Fm.	Anhydrite	MuZe	2840	0.19	36
		Kaiseraugst Fm.	Argill. Marl	MuKa	2620	0.30	23
	Bundsandstein	Dinkelberg Fm.	Sandstone	DiWeCr	2540	0.27	34
Permian	Rotliegend	Weitenau Fm.	Argill. Sandstone				
Crystalline Basement		Crystalline basement.	Crystalline basement				

258 2.2.4 Model calibration

259 The present day stress state is computed by applying the gravitational forces and lateral displacement boundary
 260 conditions to simulate the tectonic loading from the geological history. These boundary conditions are chosen
 261 so that the modeled stresses best fit the measured horizontal stress magnitude data, a process known as model
 262 calibration (Reiter and Heidbach, 2014; Ziegler and Heidbach, 2020).

263 In total, we have 30 $S_{h\min}$ and 15 $S_{h\max}$ magnitudes (Fig. 5). The $S_{h\min}$ magnitude ranges (Fig. 5: red bars) are derived
 264 from the (MHF) tests and dry sleeve reopening (SR) tests (Desroches et al., 2021a; Desroches et al., 2021b;

265 Desroches et al., 2023; Nagra, 2024d) provide the basis to bracket the ranges for the $S_{H\max}$ magnitudes (Fig. 5: 266 blue bars). However, the mean of these ranges was used for the model calibration.

267 The model calibration is done using the PyFast Calibration tool (Ziegler and Heidbach, 2021), which uses a linear 268 regression-based algorithm to compute the best-fit lateral displacement boundary conditions by minimizing the 269 differences between the modeled and measured horizontal stress magnitudes. The resulting best fit for the 270 boundary conditions of the model volume was found to be a total shortening of 0.82 m applied in the east-west 271 direction, and 4.2 m in the north-south direction. Displacements parallel to the boundaries are permitted on all 272 lateral faces of the model. At the base, vertical displacement is constrained to zero, while horizontal 273 displacement is permitted; the model top remains fully unconstrained. The numerical solution is computed using 274 the Simulia Abaqus v2021 finite element solver. The results are analyzed using Tecplot 360 EX 2023 R2 along with 275 the Geostress v2.0 add-on library (Stromeyer et al., 2020).

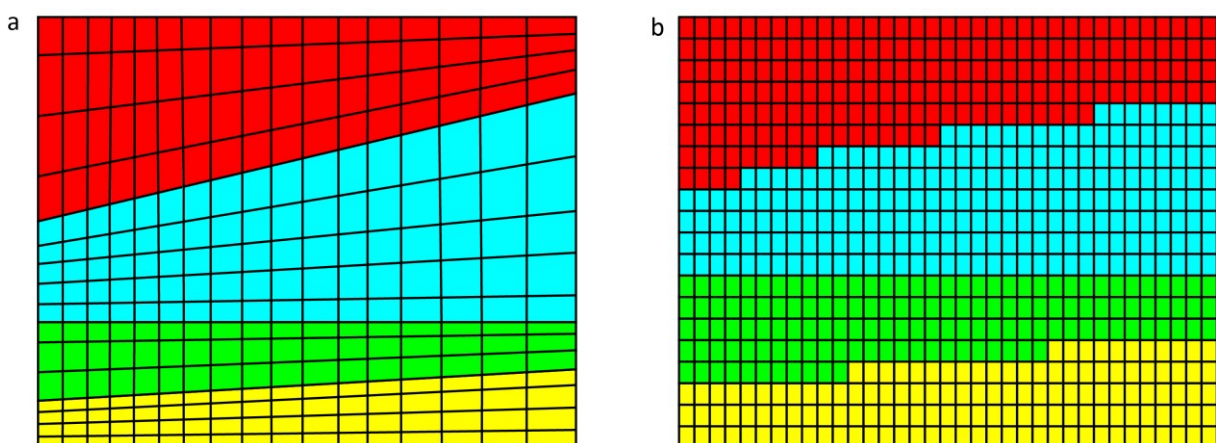
276 3. Model set-up of 3D geomechanical numerical models without fault 277 representation

278 3.1 Model discretization strategies

279 Removing the fault implementation from the 3D models allows us to use different model discretization 280 strategies, which in turn significantly accelerates the model setup and stress prediction workflow. Using two 281 different discretization strategies, we developed three additional fault-agnostic 3D geomechanical numerical 282 models. The reference model and the three fault-agnostic models are then compared to quantify the spatial 283 influence of faults on the far-field stress state. In our study, the time required to build a model was reduced from 284 approximately two months for the reference model, the model that includes contact surfaces, to just two days 285 for the fault-agnostic models.

286 The standard procedure discretizes each geomechanical unit individually using the definition of its top and 287 bottom interface surfaces, and later connected by matching the nodes along the common interfaces. Each 288 element of the unit is assigned to the appropriate mechanical properties (Fig. 4a) directly from the stratigraphic 289 definition. While this approach results in a smooth unit boundary, it requires substantial manual effort and is 290 particularly time-consuming when working with models containing many geomechanical units.

291 In order to simplify the setup and discretization procedure of the fault-agnostic models, we use ApplePy 292 (Automatic Partitioning Preventing Lengthy Manual Element Assignment), a Python-based tool that automates 293 the discretization and element property assignment process (Ziegler et al., 2020). The entire model volume is 294 discretized in a single step as a largely homogeneous mesh, ignoring both lithological interfaces and fault 295 structures. ApplePy uses the depth values of the stratigraphic boundaries to decide which element belongs to 296 which lithological unit/geomechanical unit (Fig. 4b). Although this approach introduces step-like transitions at 297 unit boundaries which looks optically unrealistic, it significantly reduces the meshing time, especially for large or 298 complex models, like the REF model without compromising the stress prediction capability of the final 3D 299 geomechanical numerical models, as discussed in Sect. 4.



301 Figure 4: A conceptual visual comparison of a) the standard procedure and b) the ApplePy procedure for discretization and
302 mechanical property assignment to geomechanical units. The four colors represent distinct geomechanical units, each with
303 unique lithologies and mechanical properties.

304 3.2 Model realizations and configurations

305 Building on the discretization strategies described in Sect. 3.1, three fault-agnostic 3D geomechanical numerical
306 model realizations were developed. The three fault-agnostic 3D geomechanical numerical models follow the
307 general model workflow of the REF model, i.e., the model parameterization and calibration are the same (Sect.
308 2.2), along with the same model extents (Sect. 2.1). They are calibrated to the same dataset of 45 horizontal
309 stress magnitude measurements used for calibrating the REF model. The only differences lie in the model
310 discretization strategies (Sect. 3.1) and finite element resolution. Out of these three models, one is set up using
311 the standard procedure, and two are set up using the ApplePy procedure. Table 2 presents the technical details
312 on the number of elements and spatial resolution of each model used, along with the corresponding best-fit
313 displacement boundary conditions obtained after applying FAST Calibration tool. The brief description of the
314 three fault-agnostic models is:

- 315 • REF-NF model: Derived directly from the REF model with identical geometry, mesh and mechanical
316 property assignments but with faults removed. Contact surfaces are eliminated, and opposing nodes
317 are equivalenced, except for the Neuhausen Fault, where a 50 m lithological offset prevents node
318 equivalencing. In this case, slip is prevented by assigning an artificially high friction coefficient of 50
- 319 • AP model: Maintains the same extents and mechanical properties as the REF and REF-NF models but
320 uses ApplePy for property assignment to the elements. It does not incorporate faults and has
321 approximately 50% more elements than the REF and REF-NF models.
- 322 • AP-H model: A higher resolution version of the AP model, with twice the number of elements. All the
323 other features of the model are the same as the AP model.

324 Table 2: Summary of technical specifications for all model realizations used in this study. Reported vertical resolutions refer
325 only to the Mesozoic units and are approximate for the ApplePy models due to depth-dependent variation. Minor differences
326 in displacement boundary conditions reflect the presence of contact surfaces in the reference model, which allow elastic
327 energy dissipation that is absent in the fault-agnostic models. The boundary conditions are compressional in nature.

Model realization	Discretization procedure	Number of elements	Vertical resolution of the mesozoic elements [m]	Lateral resolution [m]	Displacement boundary conditions	
					North-South shortening [m]	East-West shortening [m]
REF model	Standard procedure	1,923,139	5-20	100–150	4.1	0.82
REF-NF model		1,923,139	5-20	100–150	4.2	0.90
AP model	ApplePy procedure	2,826,240	~7 (non-basement units)	80–110	4.23	0.93
AP-H model		5,974,150	~4 (non-basement units)	60–80	4.25	0.90

328 4. Results

329 4.1 Stress magnitudes along borehole trajectories

330 The resulting predicted stress magnitudes from all the model realizations are presented together with the
331 measured $S_{h\min}$ (red bars) and estimated $S_{h\max}$ (blue bars) magnitude ranges along the TRU1-1 and MAR1-1
332 borehole trajectories in Fig. 5. In general, the predicted horizontal stress magnitudes from the REF model align
333 reasonably well with the measured stress ranges across different geomechanical units. However, some
334 discrepancies are present, particularly in the Klettgau and Bänkerjoch formations, where the REF model
335 underestimates $S_{h\min}$ magnitudes, and in the Schinznach formation, where $S_{h\min}$ magnitude is overestimated.
336 These deviations arise because, for the model calibration, the REF model uses P50 (median) horizontal stress
337 magnitude values despite the MHF tests resulting in ranges (red and blue bars in Fig. 5). Therefore, the stress
338 predictions may vary from the assumed P50 value at a particular point in the subsurface. The vertical stress

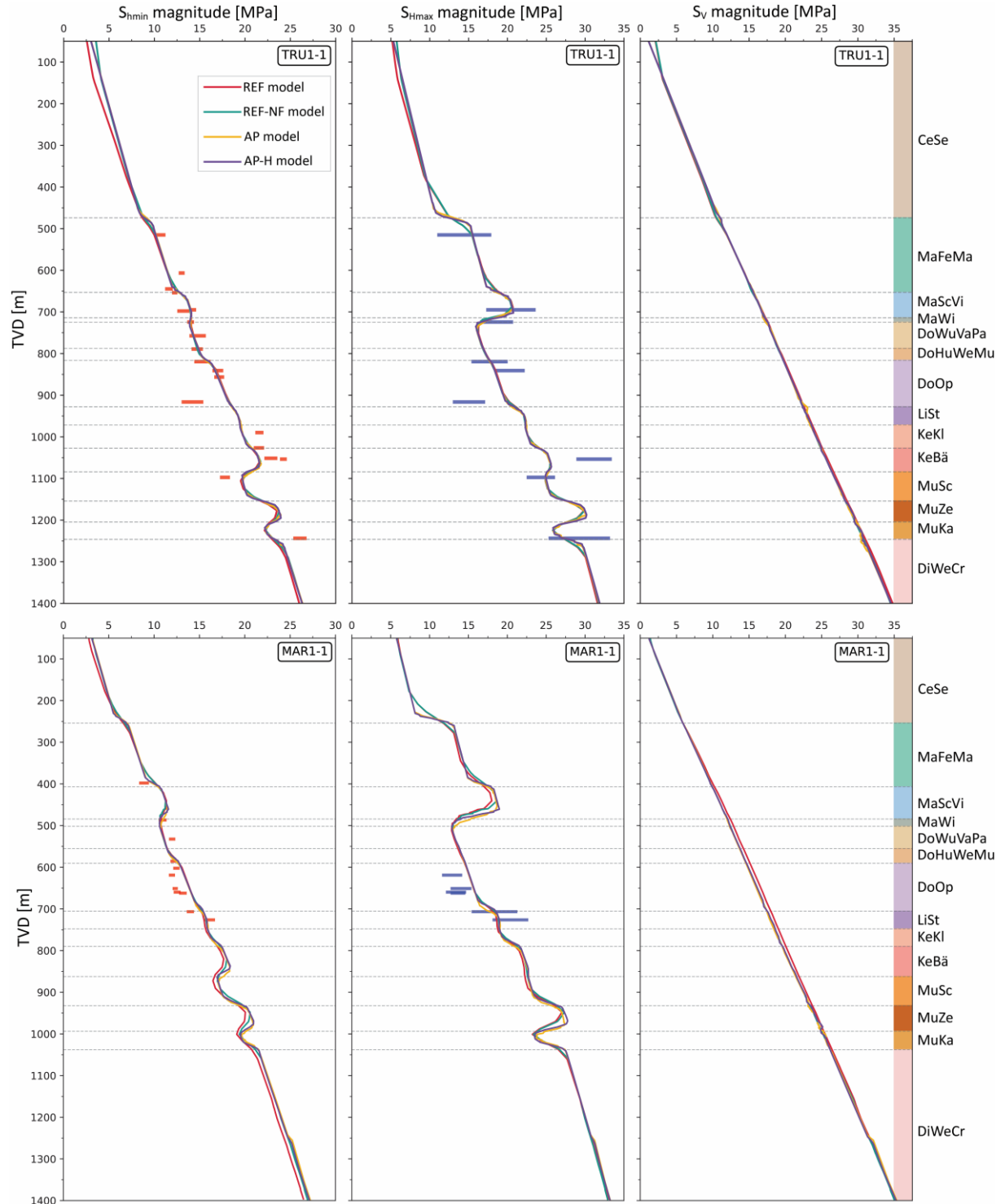
339 magnitude (S_v) is calculated from the weight of the overlying rock mass, considering the densities of the
340 individual lithologies. From Fig. 5, it can be seen that S_v increases linearly with depth.

341 The predicted results from all the model realizations, regardless of fault implementation or exclusion, also align
342 well with the measured horizontal stress magnitude ranges along both borehole trajectories across different
343 geomechanical units, and are consistent with the REF model. Minor but negligible differences of <1 MPa in the
344 $S_{H\max}$ magnitudes can be found at ~475 m (t.v.d) along the TRU1-1 borehole and at ~250 m (t.v.d) along the
345 MAR1-1 borehole in the AP and AP-H models (Fig. 5). This is likely due to a high stiffness contrast between the
346 Cenozoic sediments ($E = 15$ GPa) and Felsenkalke + Massenkalke ($E = 31$ GPa) units, the transition boundary of
347 which is differently discretized due to ApplePy usage. A similar difference can be found at the Zeglingen Fm. ($E =$
348 36 GPa), Kaiseraugst Fm. ($E = 23$ GPa) and the Dinkelberg, Weitenau Fm. and Crystalline basement ($E = 34$ GPa),
349 which is also due to the widely varying stiffness contrasts.

350 Stiffer formations such as the Schwarzbach-Villigen Fm., Zeglingen Fm., and the basement have broader stress
351 ranges in the measured data due to their statistically larger stiffness variability, while weaker formations like the
352 Opalinus Clay exhibit narrower, more consistent stress distributions. Moreover, stiffer layers shield the weaker
353 layers above and below, reducing stress variability in these formations. In short, Fig. 5 clearly indicates that the
354 differences between the profiles from all the models are smaller than the measurement errors, represented by
355 the length of the horizontal red and blue bars, and that the differences between the fault agnostic models and
356 the REF model are insignificant. The variation of S_v magnitude with depth is consistent across all the model
357 realizations, with differences <0.05 MPa observed between the models using ApplePy and the standard
358 procedure.

359 The AP and AP-H models yield identical results. This indicates that increasing model resolution would not
360 significantly improve stress predictions in our study and that the resolution of the AP model is already sufficient.
361 This rules out resolution effects within the ApplePy models on the predicted stress magnitudes with respect to
362 the REF model.

363



366 Figure 5: $S_{h\min}$ magnitude, $S_{h\max}$ magnitudes, and S_v magnitude of all the model realizations with depth (TVD) along the
 367 borehole trajectories of TRU1-1 (top row) and MAR1-1 (bottom row). The red and blue horizontal bars show the measured
 368 in-situ stress magnitude data of the $S_{h\min}$ and $S_{h\max}$, with lengths indicating their individual uncertainty (Nagra, 2024d, c). The
 369 geomechanical units are represented by their respective colors and abbreviations, consistent with Fig. 3 and Table 1.

373 4.2 Model results along a vertical cross-section and a horizontal layer

374 4.2.1 Horizontal differential stress ($S_{H\max}-S_{H\min}$)

375 Along the W-E cross-section through borehole TRU1-1, the horizontal differential stress ($S_{H\max}-S_{H\min}$) of the four
376 models displayed in Fig. 6a-d shows only small differences, except near the contact surfaces where noticeable
377 localized stress concentrations in the REF model occur. Similar result shows up when comparing the values of
378 $S_{H\max}-S_{H\min}$ along the mean Opalinus clay layer from the REF model (Fig. 6e) with those of REF-NF model (Fig. 6f).
379 To quantify the difference of the three fault-agnostic models w.r.t the REF model, Fig. 7a-c displays the difference
380 in the horizontal differential stress $\Delta(S_{H\max}-S_{H\min})$ between the models. The values of $\Delta(S_{H\max}-S_{H\min})$ exceed ± 2 MPa
381 only within 100 m of the fault. Beyond approximately 200 m from the faults, $\Delta(S_{H\max}-S_{H\min})$ across all models
382 becomes more similar to each other, and differences relative to the REF model typically remain below ± 0.4 MPa.
383 As the distance from the faults increases, the value of $\Delta(S_{H\max}-S_{H\min})$ differences rapidly decreases.

384 In addition to the spatial proximity to contact surfaces, the variation of $S_{H\max}-S_{H\min}$ depends on the stiffness of the
385 geomechanical units. In specific Mesozoic units characterized by lower stiffness, such as from the Wildegg Fm.
386 of the Malm Group to the Klettgau Fm. of the Keuper group, and the Kaiseraugst Fm. of the Muschelkalk group
387 (Table 1), the $S_{H\max}-S_{H\min}$ typically is <3.5 MPa. In contrast, units with high stiffness can exhibit $S_{H\max}-S_{H\min}$
388 exceeding 7 MPa, such as in the «Felsenkalke» + «Massenkalk» and the Schwarzbach-Villigen Fm. of the Malm
389 group, Schinznach and Zeglingen Fm. of the Muschelkalk group and the Dinkelberg Fm., Weitenau Fm. and
390 Crystalline basement (Fig. 6a-d, Table 1). This trend is expected, as lower stiffness materials accommodate
391 deformation more readily, resulting in lower differential stresses, whereas stiffer units resist deformation,
392 leading to higher differential stresses. The Opalinus Clay layer has a Young's modulus of 11 GPa, which is relatively
393 low compared to the other geomechanical units present in the siting region. The adjacent stiffer geomechanical
394 units act as stress-bearing members, effectively shielding the soft layer and further reducing the stress
395 magnitudes concentrated within it. The $S_{H\max}-S_{H\min}$ in the mean Opalinus Clay layer, as predicted by the models,
396 is <2 MPa irrespective of fault inclusion or exclusion from the model (Fig. 6e-f).

397 A particularly notable observation is that the differential stress near the Neuhausen fault remains relatively
398 comparable across all models when compared to the magnitude of differences in $S_{H\max}-S_{H\min}$ at other contact
399 surfaces. Despite the Neuhausen fault being either fully removed or mechanically disabled via a high friction
400 coefficient, the differential stress pattern across the 50-meter offset between the footwall and the hanging wall
401 is well replicated in the AP and the AP-H models in Fig. 6a-d. This is attributed to the abrupt contrast in mechanical
402 properties across the Neuhausen Fault (Fig. 3; Table 1), which effectively mimics the local stress response, even
403 in the absence of explicit fault representation.

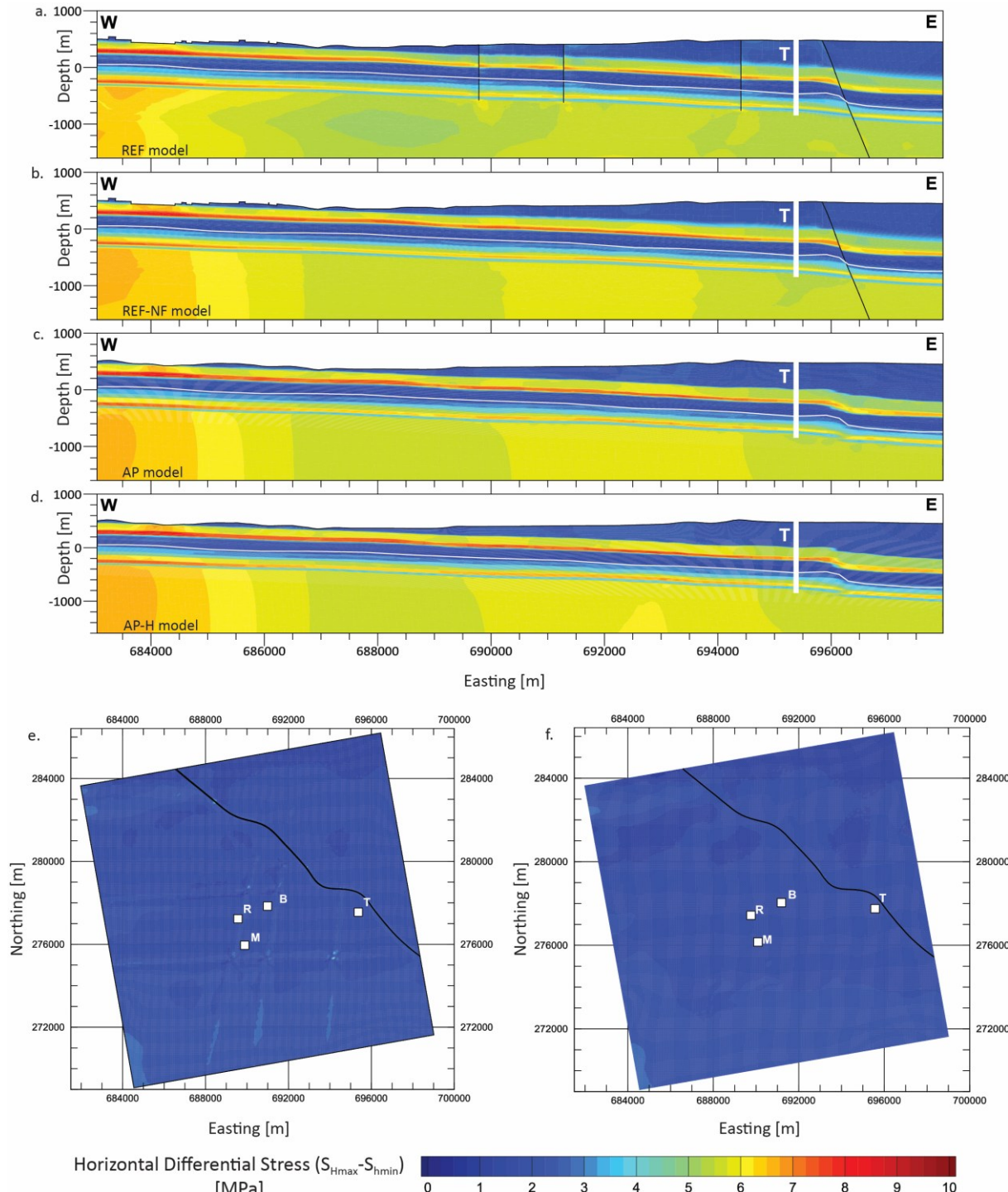
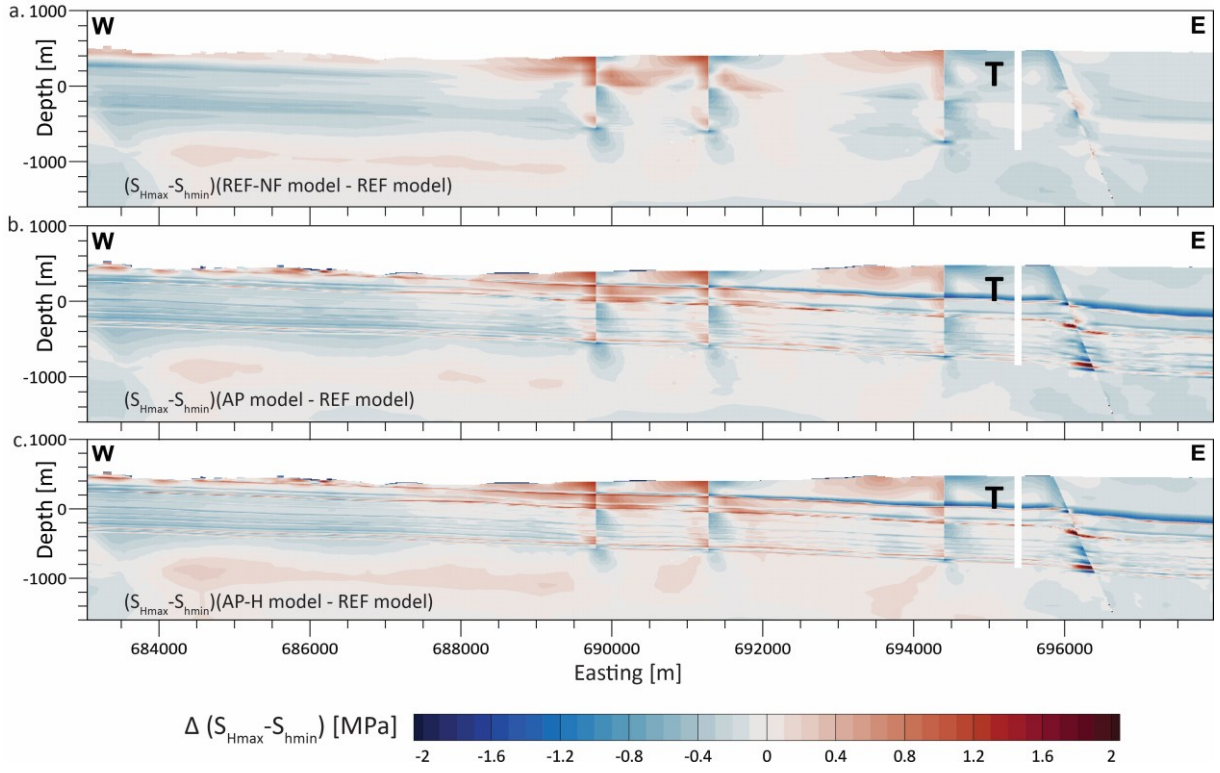


Figure 6: a-d) Modelled horizontal differential stress ($S_{h\max} - S_{h\min}$). a-d) W-E cross section (brown line in Fig. 2) through the TRU1-1 borehole (white vertical bar) with depths referenced to below sea level (b.s.l.). The location of faults is indicated by black lines. e-f) Mean Opaline Clay layer of the REF and REF-NF model, indicated by the white lines on the W-E cross sections. Capital letters indicate the location of the four boreholes TRU1-1 (T), BEN (B), MAR1-1 (M), and RHE1-1 (R).



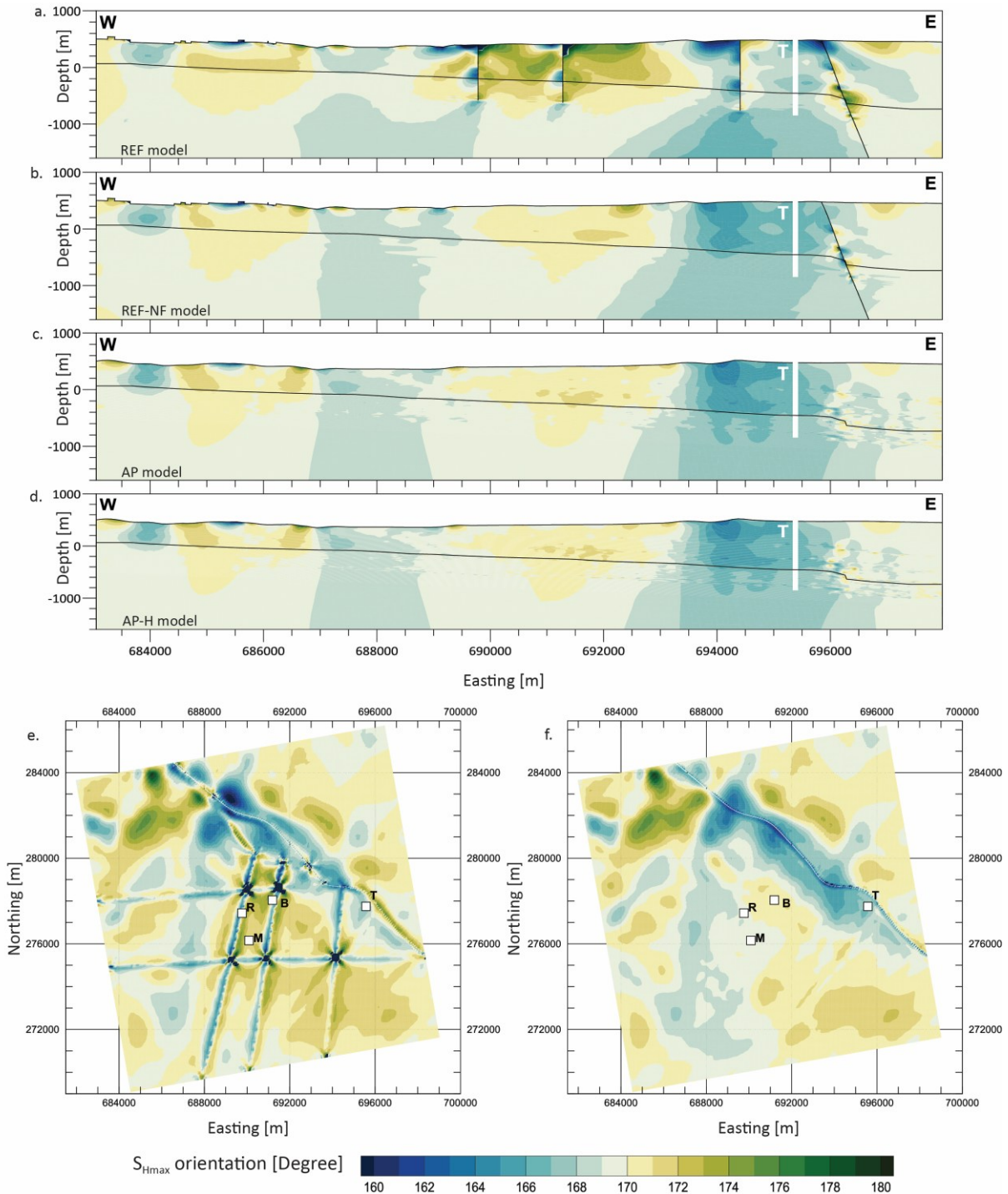
410

411 Figure 7: a-c) Difference of $S_{H\max}$ - $S_{h\min}$ between the models without faults and the REF model with active faults along the same
 412 cross-section as in Fig. 6. The cross-sections show the difference with respect to the REF model and are indicated at the
 413 bottom left of each slice. Although faults have not been directly indicated on the cross-sections, the location of the faults can
 414 be visually seen as sudden lateral changes in an otherwise continuous change in $\Delta(S_{H\max}-S_{h\min})$.

415 4.2.2 $S_{H\max}$ orientation

416 Along the same W-E cross-section as in Fig. 6a-d, the $S_{H\max}$ orientation of the four models is displayed in Fig. 8a-
 417 d, and the variability of the $S_{H\max}$ orientation w.r.t the REF model is displayed in Fig. 9a-c. Fig. 8e-f shows the
 418 variability of $S_{H\max}$ orientation along the mean Opalinus clay layer from the REF model and the REF-NF model
 419 respectively.

420 The largest $S_{H\max}$ orientation variability is reoriented more within a distance of 100–200 m around the contact
 421 surfaces, similar to the observations of $\Delta(S_{H\max}-S_{h\min})$. At this distance, differences greater than 6° w.r.t. the REF
 422 model are observed. These differences tend to reduce to less than $\pm 2^\circ$ at lateral distances greater than 500 m
 423 from the contact surfaces. Within the near-field zone, which is <300 m from the contact surfaces, stress
 424 concentrations are probably artifacts arising from the numerical resolution limit. This shift in $S_{H\max}$ orientation
 425 can also be observed in Fig. 8e-f along and near the contact surfaces. Even under a hypothetical assumption that
 426 the observed variations are entirely fault-induced, the current stress indicator techniques cannot resolve $S_{H\max}$
 427 variations within 10°. Therefore, these differences can be considered insignificant and non-resolvable. Finally,
 428 increasing model resolution does not change our results, as seen when comparing the AP and AP-H model results
 429 in Fig. 8 and Fig. 9.

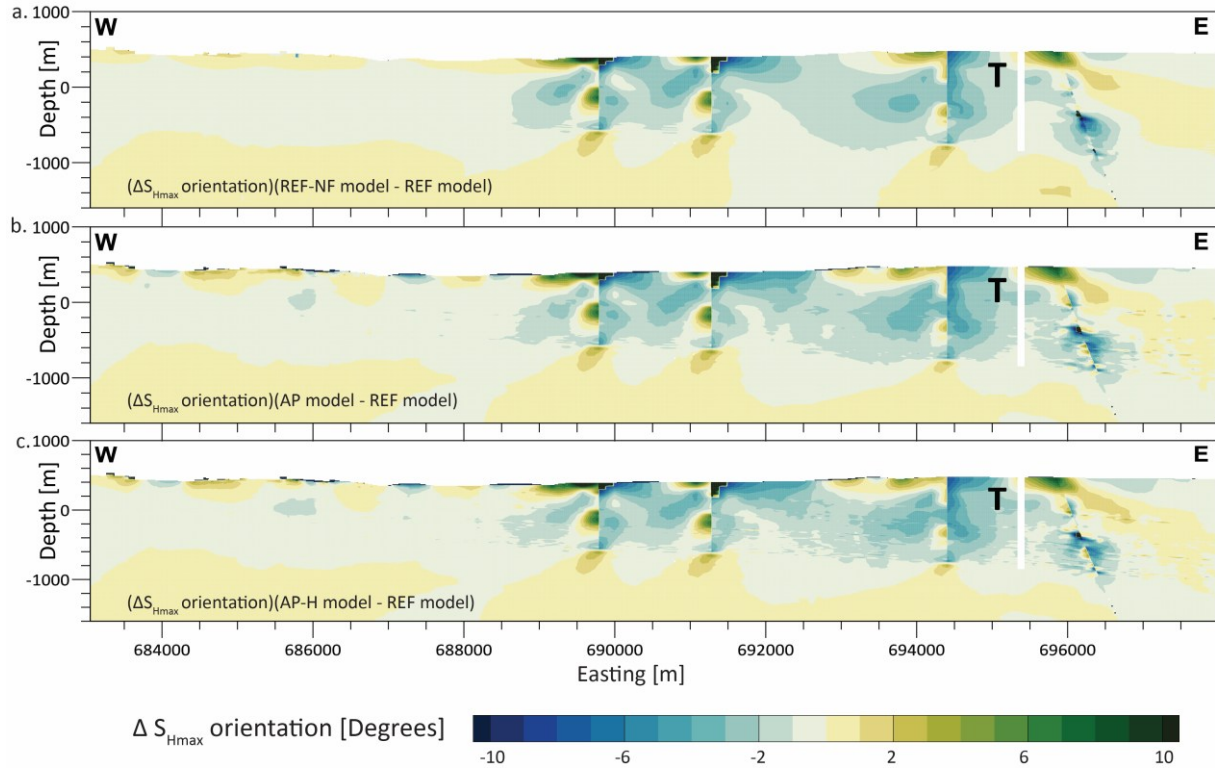


430

431 Figure 8: Absolute S_{Hmax} orientation. a-d) W-E cross-section through borehole TRU1-1 (T) indicated with the white vertical
 432 bar. e-f) Mean Opalinus Clay layer of the REF and REF-NF model, indicated by the black lines on the W-E cross sections. Capital
 433 letters indicate the location of the four boreholes TRU1-1 (T), BEN (B), MAR1-1 (M), and RHE1-1 (R).

434

435



438 Figure 9: a-c) Difference of S_{Hmax} orientation between the models without faults and the REF model with active faults along
 439 the same cross-section as in Fig. 7. The cross-sections show the difference with respect to the REF model and are indicated
 440 at the bottom left of each slice. Although faults have not been directly indicated on the cross-sections, the location of the
 441 faults can be visually seen as sudden lateral changes in an otherwise continuous change in ΔS_{Hmax} orientation.

442 4.3 Quantification of the lateral extent of fault-induced stress changes.

443 To better quantify the impact of faults on stress, we interpolated the results of the four models on a SW-NE
 444 oriented horizontal line at 300 m (b.s.l) crossing five of the seven faults (Fig. 10a-c). To improve readability, the
 445 results from the AP model were not plotted, as it is clear from Figs. 5, 7, and 9 that the AP and AP-H model results
 446 are almost identical.

447 The S_{Hmax} and S_{hmin} magnitudes of different model realizations largely overlap each other along the horizontal
 448 line. A difference of ~ 0.5 MPa is observed in S_{Hmax} magnitude (Fig. 10b), and ~ 1 MPa is observed in the S_{hmin}
 449 magnitudes (Fig. 10a) between the REF model and the fault-agnostic models, within ~ 500 m of the faults.
 450 However, these differences are less than the widths of the stress magnitude data, which in turn, represent the
 451 uncertainty of the measurements (Fig. 5). In general, the horizontal stress magnitudes from the REF model have
 452 an abrupt change in the vicinity of the faults, deviating from the continuous trend followed by other model
 453 realizations. The differences in the S_{Hmax} magnitudes reduce to < 0.2 MPa beyond a distance of about 500 m from
 454 the fault. The differences in the S_{hmin} magnitudes follow the same pattern as the S_{Hmax} magnitude, and also reduce
 455 beyond a distance of about 500 m away from the fault.

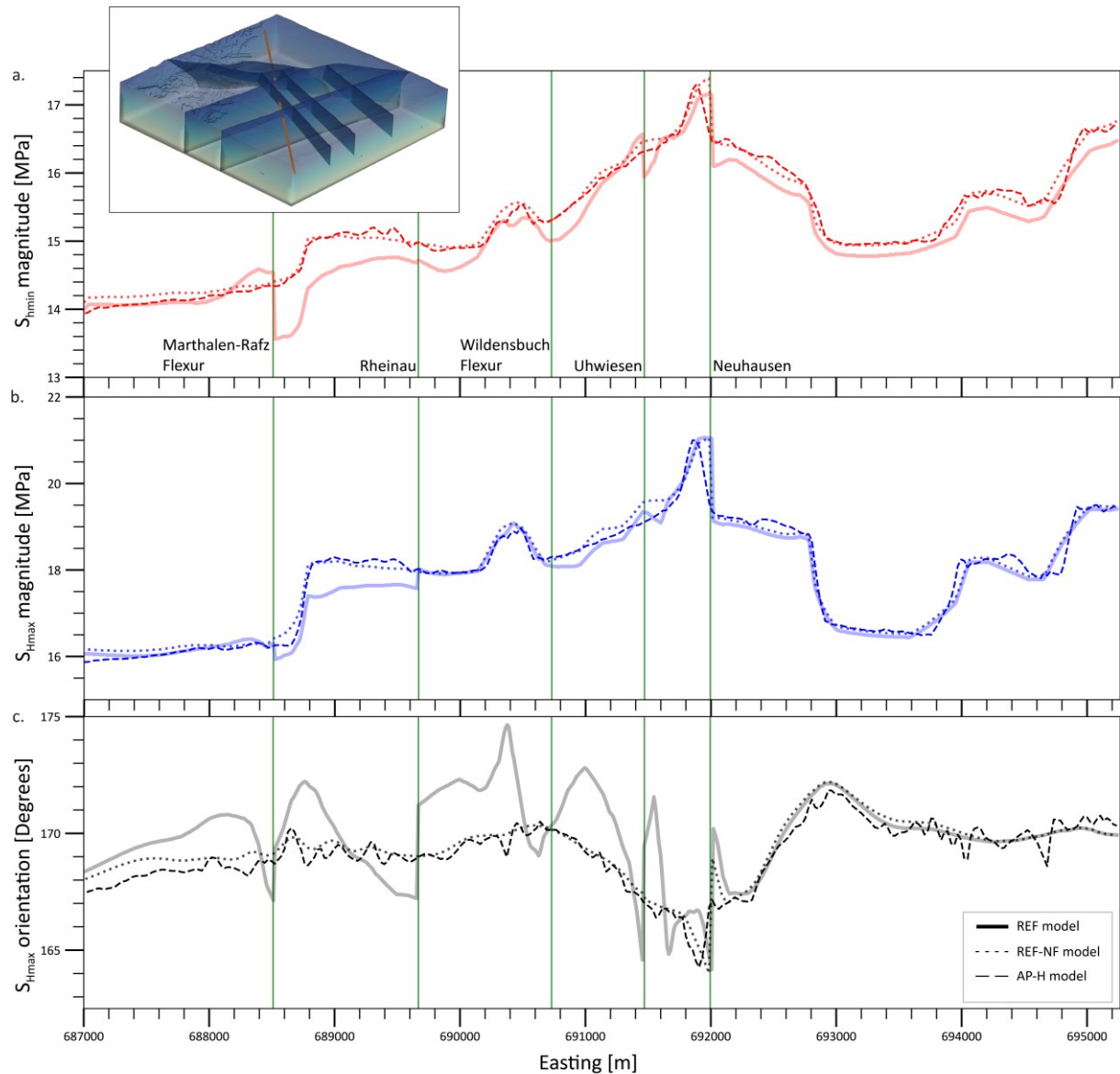
456 Similarly, the S_{Hmax} orientation of the REF model shows negligible deviations of $< 2^\circ$ in the undisturbed rock
 457 volume, away from the faults, and a deviation of 2° – 6° up to 1 km from the modeled faults (Fig. 10c). According
 458 to the quality ranking scheme of the S_{Hmax} orientation from the World Stress Map, the A-quality data, data of the
 459 highest quality, has a standard deviation of $\pm 15^\circ$ (Heidbach et al., 2025a). Even S_{Hmax} orientations derived from
 460 the DITF and BO in the MAR1-1 and TRU1-1 boreholes exhibit standard deviations of approximately $\pm 11^\circ$.
 461 Considering this, the orientation deviations seen in Fig. 10c are not resolvable and well below the uncertainties
 462 of the in situ indicators.

463 Near the Neuhausen fault, there is a localized abrupt change in the horizontal stress magnitudes within ~ 100 m
 464 on either side of the modeled fault for all the model realizations. An important observation is that this abrupt

465 change occurs not only in the REF model but also in the models without any faults. These stress changes are
 466 primarily controlled by the lateral stiffness contrasts due to the offset and not by the mere presence of the faults.

467 Overall, the differences are <0.2 MPa in stress magnitudes and <2° in $S_{H\max}$ orientations beyond 1 km from the
 468 fault, which is far less than the uncertainties of the horizontal stress magnitude data from the MHF and the SR
 469 tests, as well as the stress indicators for the $S_{H\max}$ orientation from the boreholes. Even in a conservative
 470 approach, it is clear that the effect of faults on the stress field is within about 1 km from the fault core. This
 471 conclusion aligns with the findings by Reiter et al. (2024), who, through generic model studies, found that
 472 significant stress changes due to faults only occur within a distance of a few hundred meters, partly up to 1 km
 473 next to the fault.

474



475

476 Figure 10: Magnitudes of $S_{H\min}$ and $S_{H\max}$, and the $S_{H\max}$ orientation along a SW-NE horizontal profile at 300 m (b.s.l.), shown
 477 in the 3D figure as a red line. Green vertical lines with the respective fault names denote the location where the profile crosses
 478 the modelled faults.

479

480 5. Discussion

481 5.1 Comparison with observed $S_{H\max}$ orientation data

482 The $S_{H\max}$ orientation is the most widely available characteristic of the reduced stress tensor. It is also the easiest
483 to analyze because it can be averaged and visualized with respect to the fault on stress maps (Fig. 1) (Yale et al.,
484 1993; Yale et al., 1994; Yale and Ryan, 1994; Yale, 2003; Rajabi et al., 2017c; Heidbach et al., 2018). The $S_{H\max}$
485 orientation can be determined from different stress indicators, such as from direct borehole-based indicators,
486 earthquake focal mechanisms, geological indicators, or passive seismic methods (Amadei and Stephansson,
487 1997; Zang and Stephansson, 2010; Heidbach et al., 2025a). Among these, direct borehole-based indicators such
488 as borehole breakouts (BOs), drilling-induced tensile fractures (DITFs), and hydraulic fracturing (HFs) are
489 commonly considered to be the most reliable (Bell, 1996a; Zang and Stephansson, 2010).

490 In the ZNO study region, 11 $S_{H\max}$ orientation data records are available from HFs, DITFs, and BOs. The mean $S_{H\max}$
491 orientation from these data is 170° with a standard deviation of $\pm 11^\circ$ (Nagra, 2024d, c; Heidbach et al., 2025b).
492 The individual standard deviation of each data record is between $\pm 9^\circ$ and $\pm 19^\circ$, indicating that rotations $<\pm 11^\circ$
493 cannot be resolved. As the differences between the REF model and the three fault-agnostic models, as displayed
494 in Fig. 9, are smaller than $\pm 10^\circ$, the potential impact cannot be resolved with any stress indicator. Furthermore,
495 most of the rotations observed are located close to the fault. At a distance of 1000 m from a fault, the rotation
496 is $<\pm 2^\circ$ and thus clearly below the uncertainties of any measurement.

497 The stress regime of the rock volume, by itself, would not have an influence on the $S_{H\max}$ orientation. A rotation
498 of $S_{H\max}$ orientation would primarily be driven by the horizontal differential stresses, i.e., the greater the
499 horizontal differential stresses, the lesser the possibility of any rotation in the $S_{H\max}$ orientation (Bell, 1996a;
500 Yale, 2003; Reiter et al., 2024).

501 The 1 km spatial distance limit can also be confirmed by viewing the $S_{H\max}$ orientation from the boreholes in
502 correlation with their distance from the nearest faults. The TRU1-1 borehole is less than 1 km from the
503 Neuhausen fault. Similarly, the MAR1-1 and RHE1-1 boreholes are closest to the Rheinau fault. The average $S_{H\max}$
504 orientation from the BO, DITF, and HF is $\sim 165^\circ$ along the TRU1-1 borehole, $\sim 175^\circ$ along the MAR1-1 borehole,
505 and $\sim 172.5^\circ$ along the RHE1-1 borehole (Nagra, 2024c, d). Comparing the $S_{H\max}$ orientation values from these
506 three boreholes to the regional $S_{H\max}$ orientation value of $170^\circ \pm 11^\circ$ already strengthens the argument that the
507 faults have minimal effects on $S_{H\max}$ orientation even at a distance of less than 1 km.

508 5.2 Impact of varying fault friction coefficient of the implemented faults

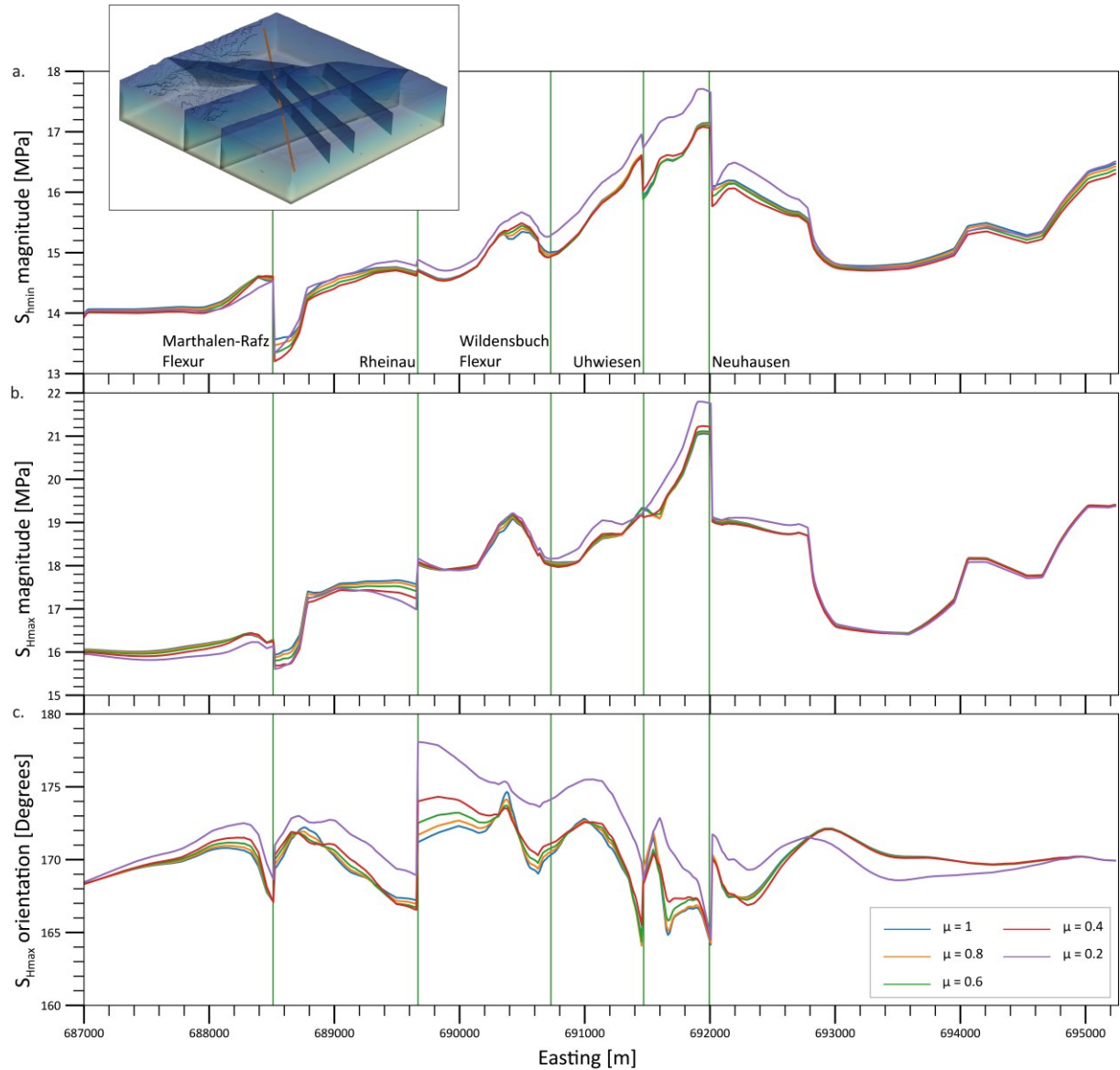
509 In geomechanical modelling, the fault strength is commonly characterized by its friction coefficient (μ) and
510 cohesion (Brandes and Tanner, 2020). In most geological settings, the friction coefficient varies between 0.6 and
511 1.0 in reservoirs with depths where normal stresses are <200 MPa on a pre-existing fracture plane (Byerlee,
512 1978; Zoback and Healy, 1984). In stark contrast, significantly lower friction coefficient values are found in
513 geological settings with extremely weak lithologies, overpressured fault cores, and in faults with very large offset
514 and/or high slip rates (Morrow et al., 1982; Morrow et al., 1992; Di Toro et al., 2011; Hergert et al., 2011; Li et
515 al., 2022). Cohesion varies with different lithologies, but for pre-existing faults, it is commonly assumed to be
516 zero. In general, the value of the friction coefficient varies between 0.4 and 0.8, and is standardly taken as 0.65
517 (Hawkes et al., 2005; Kohli and Zoback, 2013). In northern Switzerland, taking the lithology and the geological
518 setting into consideration, the values of apparent fault friction coefficient also range from 0.6 to 1.0, and very
519 rarely to 0.4 (Kastrup, 2002; Viganò et al., 2021). Kastrup (2002) states that the apparent fault friction value of
520 0.2 is extremely rare in Switzerland and only occurs at depths of more than 10 km.

521 We investigate the effect of varying the friction coefficient of the contact surfaces on the predicted in situ stress
522 state and recalibrate the REF model with a different friction coefficient. The results of stress magnitudes and
523 orientation from friction coefficients 0.2, 0.4, 0.6, and 0.8 are compared to the friction coefficient of 1.0, the
524 value we use in the REF model (Fig. 11). We see that changes in friction coefficient do not significantly affect our
525 model results beyond lateral distances of 1 km. Even within 1 km from the faults, the horizontal stress
526 magnitudes have observable variations of <1 MPa and $<5^\circ$ for the $S_{H\max}$ orientation variations. These variations
527 reduce to <0.25 MPa in both minimum and maximum horizontal stresses, and $<2.5^\circ$ in the $S_{H\max}$ orientation

528 beyond 1 km from the faults. The maximum variations, still far less than the uncertainties in the in situ stress
 529 data of the stress magnitudes and resolvable $S_{H\max}$ orientations, occur at a friction coefficient of 0.2. For the other
 530 values of the friction coefficient, the results are very much comparable to the REF model, with a friction
 531 coefficient of 1. This is to show that changing the friction coefficient has a negligible effect on the predicted
 532 stresses in our model. Minor amounts of slip, in the order of a few tens of cm, occur along the faults in the REF
 533 model during the application of boundary conditions. However, the stress change along the fault due to this slip
 534 is expected to be far less than the much larger background stresses and the differential stresses. Therefore, the
 535 minor slip occurring along the contact surfaces does not influence the overall stress field analysis.

536 These findings are in line with the results from the generic studies by Homberg et al. (1997) and Reiter et al.
 537 (2024), who studied the impact of variable friction coefficient on astress tensor and found that lower values of
 538 friction coefficient lead to a higher stress perturbation near the modelled fault. This is also seen in Fig. 11 and is
 539 because of possible decoupling at the fault and consequently a better dissipation of stress at the faults, facilitated
 540 by lower friction coefficients. The studies also showed that this effect is limited to a distance of 1 km from the
 541 fault zone.

542



543

544 Figure 11: Impact of friction coefficient (μ) on the stress tensor components. The model used here is the REF model. The
 545 results are plotted along the SW-NE horizontal profile at 300 m (b.s.l.), shown in the 3D figure as a red line. Green vertical
 546 lines with the respective fault names denote the location where the profile crosses the modelled faults.

547 5.3 Dependence of the modeling results on fault implementation

548 Faults in the REF model are represented as contact surfaces, a common and effective approach for large-scale
549 geomechanical simulations. Using contact elements to model faults seems to be a reasonable simplification for
550 large, field-scale reservoir models, where the actual width of the fault core is much smaller than the overall size
551 of the model. Hence, contact surfaces are computationally efficient for reservoir-scale models where actual fault
552 zone widths are negligible compared to model dimensions (Caine et al., 1996; Treffeisen and Henk, 2020). Since
553 our interest is on reservoir scale, alternative fault representation using, e.g. continuous rectangular finite
554 element grid, or a continuous curvilinear finite element grid in a homogenized continuum (Henk, 2009, 2020) is
555 not used in our study. Furthermore, the results from Treffeisen and Henk (2020) and Reiter et al. (2024) show
556 that the stress and strain perturbations from different technical fault implementations vary only within a few
557 tens to a few hundred meters from the fault representation. As we focus only on the far-field stress state, it can
558 be safely assumed that the choice of fault implementation approach does not significantly affect the far-field
559 results.

560 Although a numerical value does not exist for what is universally defined as far-field stresses, our model indicates
561 that at a distance of >500 m from the faults, the impact of the faults on the stress field is clearly smaller than the
562 uncertainty of the model itself and smaller than the expected variability of the stress field. As seen in Fig. 10, the
563 influence of faults on the stress field is limited to within 1 km from the contact surfaces. Beyond this distance,
564 the choice of the fault representation approach would have no significant impact on the predicted in situ stress
565 state.

566 5.4 Limitations of the study's results and future outlook

567 In the REF model, the faults, represented by contact surfaces, are simplified and a unified representation of
568 numerous small fault patches that were interpreted from the 3D seismic interpretation. This simplification is
569 necessary for an easier and reasonable representation of fault structures and the consequent computational
570 simulation feasibility of the model. However, the reality is more complex. In the subsurface, faults often occur in
571 clusters and display heterogeneous geometry, composition, and structure (Tanner and Brandes, 2020). Large
572 faults are often accompanied by zones of secondary faults, which can extend the spatial influence of faults on
573 the stress state. Small fault segments of the primary fault and the associated secondary faults can lead to a higher
574 stress concentration along the fault surfaces, complicating the interaction between faults and the in situ stresses
575 (Jones, 1988; Maerten et al., 2002). A single fault may also have complex geometry with multiple bends (Saucier
576 et al., 1992; Roche et al., 2021), increasing its influence on stresses compared to the planar faults.

577 Our study focuses on a reservoir scale, in the order of a few km, to predict present day stress variation in the
578 area of interest. While seven faults were implemented in the REF model, many more fractures or joints exist in
579 reality but cannot be resolved at our current lateral resolution of approximately 70–100 m, and the available
580 structural geological data. Including these would significantly increase the element count and computational
581 demand, far beyond the scope or need of most studies. It is important to emphasize that the focus of our results
582 is only the far-field present day stresses, and in an intact and undisturbed rock volume.

583 While previous studies have documented significant stress rotations near fault tips, they also emphasize that
584 these perturbations are typically localized, rarely extending beyond a few hundred meters from the termination
585 point (Homberg et al., 1997; Nicol et al., 2020). Our findings are in general agreement with this observation. In
586 our model, fault tips ending within the Mesozoic sediments indeed exhibit localized stress concentrations and
587 enhanced stress rotations. However, because these effects are spatially restricted, they do not significantly alter
588 the regional stress field predicted by the fault-agnostic models at distances greater than a few 100 m from the
589 structural discontinuities.

590 Extreme cases exist where large-scale faulting separated the crust into distinct fault blocks, each having an
591 independent $S_{H\max}$ orientation between adjacent fault blocks of the same field (Yale et al., 1994; Yale and Ryan,
592 1994; Bell, 1996b; Kattenhorn et al., 2000; Hergert and Heidbach, 2011; Hergert et al., 2011; Li et al., 2019; Qin
593 et al., 2024). While complex stress patterns and large $S_{H\max}$ rotations have been reported for major fault systems
594 such as the Møre–Trøndelag Fault Complex and the San Andreas Fault, these systems differ fundamentally from
595 the Alpine Foreland Basin in terms of tectonic setting, fault displacement magnitude, and fault frictional

596 properties (Zoback et al., 1987; Pascal and Gabrielsen, 2001; Roberts and Myrvang, 2004). In particular, the large
597 offsets and anomalously low friction coefficients reported for these systems are not representative of the fault
598 conditions in northern Switzerland. But, as seen in our study region, if the Mesozoic sediments are not massively
599 faulted or fractured, have sufficiently large differential stresses, and are located in an intraplate Foreland Basin
600 setting, it could be expected that the impact of faults on the stress state would only be within 1 km from the
601 fault zone. However, further investigation is needed for other geological settings, with different lithologies such
602 as salt domes, anhydrite, or crystalline rock formations, or regions where faults exhibit more complex geometry
603 with more curvature/ bends, or with extremely large total offsets and high slip rates, to confirm the broader
604 applicability of our results.

605 6. Conclusion

606 We evaluated the influence of faults on the regional stress state using 3D geomechanical models of the Zürich
607 Nordost siting region, which are calibrated on a robust dataset of 30 minimum horizontal and 15 maximum
608 horizontal stress magnitudes from two boreholes. We directly compare the predicted stress states between
609 models where faults have been modelled as contact surfaces and models where faults have been excluded or
610 mechanically deactivated. Our findings show that faults cause only local stress perturbations, within 500 m from
611 the contact surfaces, with their impact becoming negligible beyond 1 km from the fault. At this scale, stress
612 variations are mainly controlled by contrasts in rock stiffness on the juxtaposed formations rather than just the
613 relative mechanical weakness presented by the fault plane. The variations between the model realizations must
614 also be viewed in conjunction with the rock stress variability, which in turn results from stiffness variability. The
615 fault-induced stress effects at distances >1 km are smaller than the typical resolution limits of stress data and
616 uncertainties of the stress magnitude measurements, which are $\pm 11^\circ$ for $S_{H\max}$ orientation and 0.7–3.5 MPa for
617 stress magnitude, derived from the description of stress magnitudes as ranges. Importantly, omitting faults from
618 the modeling workflow can reduce model setup and computational time from months to 1–2 days using
619 alternative discretization strategies, without sacrificing stress prediction reliability. These findings provide
620 valuable guidance for efficient and reliable reservoir-scale geomechanical modeling, including site assessments
621 for a deep geological repository, where predicting far-field in situ stresses in intact rock volumes is essential,
622 given that the storage sites are located away from active faults (>1 km) in an intact and undisturbed rock volume.
623 However, further studies in different geologic settings and under different stress conditions are required to verify
624 the general applicability of our results from northern Switzerland.

625 Author contribution

626 LSARV: Conceptualization, Formal analysis, Methodology, Model preparation, Validation, Visualization, Writing
627 (original draft preparation), and Writing (review and editing).

628 OH: Conceptualization, Data curation, Funding acquisition, Project administration, Resources, Supervision,
629 Validation, and Writing (review and editing).

630 MZ: Resources, Software, Supervision, Validation, and Writing (review and editing).

631 KR: Methodology, Resources, Model preparation, Validation, and Writing (review and editing), Funding
632 acquisition.

633 AH: Funding acquisition, Project administration, and Writing (review and editing).

634 MR: Conceptualization, Visualization, Writing (review and editing).

635 SBG: Resources, and Writing (review and editing).

636 TH: Visualization, Writing (review and editing).

637 Competing Interests

638 The authors declare that they have no conflict of interest.

639 Disclaimer

640 Publisher's note: Copernicus Publications remains neutral with regard to jurisdictional claims made in the text,
641 published maps, institutional affiliations, or any other geographical representation in this paper. While
642 Copernicus Publications makes every effort to include appropriate place names, the final responsibility lies with
643 the authors.

644 Acknowledgements

645 We thank NAGRA for providing access to the extensive dataset used in our study. We also thank SQuaRe and
646 SpannEnd 2.0 for the funding.

647 Financial support

648 The authors gratefully acknowledge the funding provided by the Bundesministerium für Umwelt, Naturschutz,
649 nukleare Sicherheit und Verbraucherschutz through the project SQuaRe (project number: 02E12062B), and by
650 the Bundesgesellschaft für Endlagerung (BGE) through the project SpannEnD 2.0 (<https://www.spannend-projekt.de>). Additional support was provided by the National Cooperative for the Disposal of Radioactive Waste
651 (Nagra), Switzerland.

653 References

654 Ahlers, S., Henk, A., Hergert, T., Reiter, K., Müller, B., Röckel, L., Heidbach, O., Morawietz, S., Scheck-
655 Wenderoth, M., and Anikiev, D.: 3D crustal stress state of Germany according to a data-calibrated geomechanical
656 model, *Solid Earth*, 12, 1777–1799, <https://doi.org/10.5194/se-12-1777-2021>, 2021.

657 Ahlers, S., Röckel, L., Hergert, T., Reiter, K., Heidbach, O., Henk, A., Müller, B., Morawietz, S., Scheck-
658 Wenderoth, M., and Anikiev, D.: The crustal stress field of Germany: a refined prediction, *Geothermal Energy*,
659 10, 10, <https://doi.org/10.1186/s40517-022-00222-6>, 2022.

660 Aleksandrowski, P., Inderhaug, O. H. E., and Knapstad, B.: Tectonic structures and wellbore breakout orientation,
661 The 33rd U.S. Symposium on Rock Mechanics (USRMS), Santa Fe, New Mexico, USA, 3–5 June,
662 [https://doi.org/10.1016/0148-9062\(93\)90652-T](https://doi.org/10.1016/0148-9062(93)90652-T), 1992.

663 Amadei, B. and Stephansson, O.: Rock stress and its measurement, Springer Dordrecht,
664 <https://doi.org/10.1007/978-94-011-5346-1>, 1997.

665 Azzola, J., Valley, B., Schmittbuhl, J., and Genter, A.: Stress characterization and temporal evolution of borehole
666 failure at the Rittershoffen geothermal project, *Solid Earth*, 10, 1155–1180, <https://doi.org/10.5194/se-10-1155-2019>, 2019.

668 Barton, C. A. and Zoback, M. D.: Stress perturbations associated with active faults penetrated by boreholes:
669 Possible evidence for near-complete stress drop and a new technique for stress magnitude measurement, *Journal
670 of Geophysical Research: Solid Earth*, 99, 9373–9390, <https://doi.org/10.1029/93JB03359>, 1994.

671 Bell, J. S.: Petro Geoscience 1. In situ stresses in sedimentary rocks (Part 1): Measurement Techniques, *Geoscience
672 Canada*, 23, 1996a.

673 Bell, J. S.: Petro Geoscience 2. In-Situ Stresses in Sedimentary Rocks (Part 2): Application of Stress
674 Measurements, *Geoscience Canada*, 23, 135–153, 1996b.

675 Bell, J. S. and Gough, D. I.: Northeast-southwest compressive stress in Alberta evidence from oil wells, *Earth and
676 Planetary Science Letters*, 45, 475–482, [https://doi.org/10.1016/0012-821X\(79\)90146-8](https://doi.org/10.1016/0012-821X(79)90146-8), 1979.

677 Bell, J. S. and Grasby, S. E.: The stress regime of the Western Canadian Sedimentary Basin, *Geofluids*, 12, 150–
678 165, <https://doi.org/10.1111/j.1468-8123.2011.00349.x>, 2012.

679 Bérard, T. and Desroches, J.: Geological structure, geomechanical perturbations, and variability in hydraulic
680 fracturing performance at the scale of a square mile, *Geomechanics for Energy and the Environment*, 26, 100137,
681 <https://doi.org/10.1016/j.gete.2019.100137>, 2021.

682 Berard, T., Sinha, B. K., Van Ruth, P., Dance, T., John, Z., and Tan, C.: Stress estimation at the Otway CO₂
683 storage site, Australia, *SPE Asia Pacific Oil and Gas Conference and Exhibition*, Perth, Australia,
684 <https://doi.org/10.2118/116422-MS>, 2008.

685 Boness, N. L. and Zoback, M. D.: A multiscale study of the mechanisms controlling shear velocity anisotropy in
686 the San Andreas Fault Observatory at Depth, *GEOPHYSICS*, 71, F131–F146, <https://doi.org/10.1190/1.2231107>,
687 2006.

688 Brandes, C. and Tanner, D. C.: Chapter 2 - Fault mechanics and earthquakes, in: *Understanding Faults*, edited by:
689 Tanner, D., and Brandes, C., Elsevier, 11–80, <https://doi.org/10.1016/B978-0-12-815985-9.00002-3>, 2020.

690 Brodsky, E. E., Mori, J. J., Anderson, L., Chester, F. M., Conin, M., Dunham, E. M., Eguchi, N., Fulton, P. M.,
691 Hino, R., Hirose, T., Ikari, M. J., Ishikawa, T., Jeppson, T., Kano, Y., Kirkpatrick, J., Kodaira, S., Lin, W.,
692 Nakamura, Y., Rabinowitz, H. S., Regalla, C., Remitti, F., Rowe, C., Saffer, D. M., Saito, S., Sample, J., Sanada,
693 Y., Savage, H. M., Sun, T., Toczko, S., Ujiie, K., Wolfson-Schwehr, M., and Yang, T.: The State of Stress on the
694 Fault Before, During, and After a Major Earthquake, *Annual Review of Earth and Planetary Sciences*, 48, 49–74,
695 <https://doi.org/10.1146/annurev-earth-053018-060507>, 2020.

696 Brooke-Barnett, S., Flottmann, T., Paul, P. K., Busetti, S., Hennings, P., Reid, R., and Rosenbaum, G.: Influence
697 of basement structures on in situ stresses over the Surat Basin, southeast Queensland, *Journal of Geophysical
698 Research: Solid Earth*, 120, 4946–4965, <https://doi.org/10.1002/2015JB011964>, 2015.

699 Brudy, M., Fuchs, K., and Zoback, M. D.: Stress orientation profile to 6 km depth in the KTB main borehole, KTB
700 Report 93-2: Contributions to the 6. Annual KTB-Colloquium, Geoscientific Results, Giessen, Germany, 1–2 June,
701 195–197, <https://doi.org/10.2312/KTB.93-2>, 1992.

702 Brudy, M., Zoback, M. D., Fuchs, K., Rummel, F., and Baumgärtner, J.: Estimation of the complete stress tensor
703 to 8 km depth in the KTB scientific drill holes: Implications for crustal strength, *Journal of Geophysical Research: Solid Earth*, 102, 18453–18475, <https://doi.org/10.1029/96JB02942>, 1997.

705 Buchmann, T. J. and Connolly, P. T.: Contemporary kinematics of the Upper Rhine Graben: A 3D finite element
706 approach, *Global and Planetary Change*, 58, 287–309, <https://doi.org/10.1016/j.gloplacha.2007.02.012>, 2007.

707 Burkhard, M. and Sommaruga, S.: Evolution of the western Swiss Molasse basin: structural relations with the Alps
708 and the Jura belt, *Geological Society, London, Special Publications*, 134, 279–298,
709 <https://doi.org/10.1144/GSL.SP.1998.134.01.13>, 1998.

710 Byerlee, J.: Friction of rocks, *pure and applied geophysics*, 116, 615–626, <https://doi.org/10.1007/BF00876528>,
711 1978.

712 Caine, J. S., Evans, J. P., and Forster, C. B.: Fault zone architecture and permeability structure, *Geology*, 24, 1025–
713 1028, [https://doi.org/10.1130/0091-7613\(1996\)024%3C1025:FZAAPS%3E2.3.CO;2](https://doi.org/10.1130/0091-7613(1996)024%3C1025:FZAAPS%3E2.3.CO;2), 1996.

714 Catalli, F., Meier, M.-A., and Wiemer, S.: The role of Coulomb stress changes for injection-induced seismicity:
715 The Basel enhanced geothermal system, *Geophysical Research Letters*, 40, 72–77,
716 <https://doi.org/10.1029/2012GL054147>, 2013.

717 Chéry, J., Zoback, M. D., and Hickman, S.: A mechanical model of the San Andreas fault and SAFOD Pilot Hole
718 stress measurements, *Geophysical Research Letters*, 31, <https://doi.org/10.1029/2004GL019521>, 2004.

719 Cloetingh, S., Cornu, T., Ziegler, P. A., and Beekman, F.: Neotectonics and intraplate continental topography of
720 the northern Alpine Foreland, *Earth-Science Reviews*, 74, 127–196,
721 <https://doi.org/10.1016/j.earscirev.2005.06.001>, 2006.

722 Cloetingh, S. and Wortel, R.: Regional stress field of the Indian Plate, *Geophysical Research Letters*, 12, 77–80,
723 <https://doi.org/10.1029/GL012i002p00077>, 1985.

724 Coward, M. and Dietrich, D.: Alpine tectonics — an overview, Geological Society, London, Special Publications, 725 45, 1–29, <https://doi.org/10.1144/GSL.SP.1989.045.01.0>, 1989.

726 Desroches, J., Peyret, E., Gisolf, A., Wilcox, A., Di Giovanni`i, M., de Jong, A. S., Sepehri, S., Garrard, R., and 727 Giger, S.: Stress Measurement Campaign in Scientific Deep Boreholes: Focus on Tools and Methods, *Petrophysics* 728 - The SPWLA Journal, 64, 621–639, <https://doi.org/10.30632/PJV64N5-2023a2>, 2023.

729 Desroches, J., Peyret, E., Gisolf, A., Wilcox, A., Di Giovanni, M., de Jong, A. S., Sepehri, S., Garrard, R., and 730 Giger, S.: Stress Measurement Campaign in Scientific Deep Boreholes: Focus on Tool and Methods, *SPWLA* 731 62nd Annual Logging Symposium, Virtual Event, 17–20 May, <https://doi.org/10.30632/SPWLA-2021-0056>, 732 2021a.

733 Desroches, J., Peyret, E., Gisolf, A., Wilcox, A., Di Giovanni, M., Schram de Jong, A., Milos, B., Gonus, J., 734 Bailey, E., Sepehri, S., Garitte, B., Garrard, R., and Giger, S.: Stress-Measurement Campaign in Scientific Deep 735 Boreholes: From Planning to Interpretation, 55th U.S. Rock Mechanics/Geomechanics Symposium, Virtual Event, 736 20–23 June, 2021b.

737 Di Toro, G., Han, R., Hirose, T., De Paola, N., Nielsen, S., Mizoguchi, K., Ferri, F., Cocco, M., and Shimamoto, 738 T.: Fault lubrication during earthquakes, *Nature*, 471, 494–498, <https://doi.org/10.1038/nature09838>, 2011.

739 Diebold, P. and Noack, T.: Late Palaeozoic troughs and Tertiary structures in the eastern Folded Jura, in: *Deep* 740 *Structure of the Swiss Alps: Results of NRP20*, edited by: Pfiffner, O. A., Lehner, P., Heitzmann, P., Mueller, S., 741 and Steck, A., Birkhäuser Verlag, Basel, 59–63, 1997.

742 Fiebig, M. and Preusser, F.: Pleistocene glaciations of the northern Alpine Foreland, *Geographica Helvetica*, 63, 743 145–150, <https://doi.org/10.5194/gh-63-145-2008>, 2008.

744 Fischer, K. and Henk, A.: A workflow for building and calibrating 3-D geomechanical models- a case study for a 745 gas reservoir in the North German Basin, *Solid Earth*, 4, 347–355, <https://doi.org/10.5194/se-4-347-2013>, 2013.

746 Gens, A., Garitte, B., Olivella, S., and Vaunat, J.: Applications of multiphysical geomechanics in underground 747 nuclear waste storage, *European Journal of Environmental and Civil Engineering*, 13, 7–8, 748 <https://doi.org/10.1080/19648189.2009.9693162>, 2009.

749 Gorin, G., Signer, C., and Amberger, G.: Structural configuration of the western Swiss Molasse Basin as defined 750 by reflection seismic data, *Eclogae Geologicae Helvetiae*, 86, 693–716, 1993.

751 Gough, D. I. and Bell, J. S.: Stress orientations from borehole wall fractures with examples from Colorado, east 752 Texas, and northern Canada, *Canadian Journal of Earth Sciences*, 19, 1358–1370, <https://doi.org/10.1139/e82-118>, 753 1982.

754 Hawkes, C., McLellan, P., and Bachu, S.: Geomechanical factors affecting geological storage of CO₂ in depleted 755 oil and gas reservoirs, *Journal of Canadian Petroleum Technology*, 44, 2005.

756 Heidbach, O., Rajabi, M., Cui, X., Fuchs, K., Müller, B., Reinecker, J., Reiter, K., Tingay, M., Wenzel, F., Xie, 757 F., Ziegler, M. O., Zoback, M.-L., and Zoback, M.: The World Stress Map database release 2016: Crustal stress 758 pattern across scales, *Tectonophysics*, 744, 484–498, <https://doi.org/10.1016/j.tecto.2018.07.007>, 2018.

759 Heidbach, O., Rajabi, M., Di Giacomo, D., Harris, J., Lammers, S., Morawietz, S., Pierdominici, S., Reiter, K., 760 Storchak, D., von Specht, S., and Ziegler, M. O.: World Stress Map Database Release 2025, 761 <https://doi.org/10.5880/WSM.2025.001>, 2025a.

762 Heidbach, O., Reinecker, J., Diehl, T., Desroches, J., Ziegler, M. O., Reiter, K., Vietor, T., and Giger, S. B.: The 763 present-day crustal stress field of the Molasse Basin in Switzerland, *Swiss Journal of Geosciences*, 764 <https://doi.org/10.1186/s00015-025-00487-6>, 2025b.

765 Heidbach, O., Reinecker, J., Tingay, M., Müller, B., Sperner, B., Fuchs, K., and Wenzel, F.: Plate boundary forces 766 are not enough: Second- and third-order stress patterns highlighted in the World Stress Map database, *Tectonics*, 767 26, TC6014, <https://doi.org/10.1029/2007TC002133>, 2007.

768 Henk, A.: Pre-drilling prediction of the tectonic stress field with geomechanical models, *First Break*, 23, 53–57,
769 <https://doi.org/10.3997/1365-2397.2005021>, 2005.

770 Henk, A.: Perspectives of Geomechanical Reservoir Models - Why Stress is Important, *Oil Gas European*
771 Magazine, 35(1), 20–24, 2009.

772 Henk, A.: Chapter 4 - Numerical modelling of faults, in: *Understanding Faults*, edited by: Tanner, D., and Brandes,
773 C., Elsevier, 147–165, <https://doi.org/10.1016/B978-0-12-815985-9.00004-7>, 2020.

774 Hergert, T. and Heidbach, O.: Geomechanical model of the Marmara Sea region—II. 3-D contemporary
775 background stress field, *Geophysical Journal International*, 185, 1090–1102, <https://doi.org/10.1111/j.1365-246X.2011.04992.x>, 2011.

777 Hergert, T., Heidbach, O., Bécel, A., and Laigle, M.: Geomechanical model of the Marmara Sea region - I. 3-D
778 contemporary kinematics, *Geophysical Journal International*, 185, 1073–1089, <https://doi.org/10.1111/j.1365-246X.2011.04991.x>, 2011.

780 Hergert, T., Heidbach, O., Reiter, K., Giger, S. B., and Marschall, P.: Stress field sensitivity analysis in a
781 sedimentary sequence of the Alpine foreland, northern Switzerland, *Solid Earth*, 6, 533–552,
782 <https://doi.org/10.5194/se-6-533-2015>, 2015.

783 Hickman, S. and Zoback, M.: Stress orientations and magnitudes in the SAFOD pilot hole, *Geophysical Research*
784 Letters, 31, <https://doi.org/10.1029/2004GL020043>, 2004.

785 Homberg, C., Hu, J. C., Angelier, J., Bergerat, F., and Lacombe, O.: Characterization of stress perturbations near
786 major fault zones: insights from 2-D distinct-element numerical modelling and field studies (Jura mountains),
787 *Journal of Structural Geology*, 19, 703–718, [https://doi.org/10.1016/S0191-8141\(96\)00104-6](https://doi.org/10.1016/S0191-8141(96)00104-6), 1997.

788 Illies, J. H.: The Rhine graben rift system-plate tectonics and transform faulting, *Geophysical surveys*, 1, 27–60,
789 <https://doi.org/10.1007/BF01449550>, 1972.

790 Jaeger, J. C., Cook, N. G. W., and Zimmerman, R. W.: *Fundamentals of Rock Mechanics*, 4, Blackwell Publishing,
791 2007.

792 Jo, Y., Chang, C., Ji, S.-H., and Park, K.-W.: In situ stress states at KURT, an underground research laboratory in
793 South Korea for the study of high-level radioactive waste disposal, *Engineering Geology*, 259, 105198,
794 <https://doi.org/10.1016/j.enggeo.2019.105198>, 2019.

795 Jones, W. B.: Listric growth faults in the Kenya Rift Valley, *Journal of Structural Geology*, 10, 661–672,
796 [https://doi.org/10.1016/0191-8141\(88\)90074-0](https://doi.org/10.1016/0191-8141(88)90074-0), 1988.

797 Jordan, P.: Triassic. Basin evolution: Switzerland., in: *The Geology of Central Europe. Volume 2: Mesozoic and*
798 *Cenozoic*, edited by: McCann, T., Geological Society of London, London, 785–788,
799 <https://doi.org/10.1144/CEV2P>, 2008.

800 Kastrup, U.: Seismotectonics and Stress Field Variations in Switzerland, Dissertation, Swiss Federal Institute of
801 Technology Zurich (ETH Zurich), Zurich, 162 pp., <https://doi.org/10.3929/ethz-a-004423062>, 2002.

802 Kattenhorn, S. A., Aydin, A., and Pollard, D. D.: Joints at high angles to normal fault strike: an explanation using
803 3-D numerical models of fault-perturbed stress fields, *Journal of Structural Geology*, 22, 1–23,
804 [https://doi.org/10.1016/S0191-8141\(99\)00130-3](https://doi.org/10.1016/S0191-8141(99)00130-3), 2000.

805 Kempf, O. and Adrian, P., O.: Early Tertiary evolution of the North Alpine Foreland Basin of the Swiss Alps and
806 adjoining areas, *Basin Research*, 16, 549–567, <https://doi.org/10.1111/j.1365-2117.2004.00246.x>, 2004.

807 Kingsborough, R. H., Williams, A. F., and Hillis, R. R.: Borehole Instability on the Northwest Shelf of Australia,
808 SPE Asia-Pacific Conference, Perth, Australia, 4–7 Nov, <https://doi.org/10.2118/23015-MS>, 1991.

809 Kohli, A. H. and Zoback, M. D.: Frictional properties of shale reservoir rocks, *Journal of Geophysical Research: Solid Earth*, 118, 5109–5125, <https://doi.org/10.1002/jgrb.50346>, 2013.

811 Laubscher, H.: Jura, Alps and the boundary of the Adria subplate, *Tectonophysics*, 483, 223–239,
812 <https://doi.org/10.1016/j.tecto.2009.10.011>, 2010.

813 Lecampion, B. and Lei, T.: Reconstructing the 3D Initial Stress State over Reservoir Geomechanics Model from
814 Local Measurements and Geological Priors: A Bayesian Approach, *Schlumberger J. of Modeling, Design and*
815 *Simulation*, 1, 100–104, <https://infoscience.epfl.ch/handle/20.500.14299/119734>, 2010.

816 Li, P., Cai, M.-f., Miao, S.-j., and Guo, Q.-f.: New Insights Into The Current Stress Field Around the Yishu Fault
817 Zone, Eastern China, *Rock Mechanics and Rock Engineering*, 52, 4133–4145, <https://doi.org/10.1007/s00603-019-01792-x>, 2019.

819 Li, X., Hergert, T., Henk, A., and Zeng, Z.: Contemporary background stress field in the eastern Tibetan Plateau:
820 Insights from 3D geomechanical modeling, *Tectonophysics*, 822, 229177,
821 <https://doi.org/10.1016/j.tecto.2021.229177>, 2022.

822 Long, J. C. S. and Ewing, R. C.: YUCCA MOUNTAIN: Earth-Science Issues at a Geologic Repository for High-
823 Level Nuclear Waste, *Annual Review of Earth and Planetary Sciences*, 32, 363–401,
824 <https://doi.org/10.1146/annurev.earth.32.092203.122444>, 2004.

825 Madritsch, H., Looser, N., Schneeberger, R., Wohlwend, S., Guillong, M., and Malz, A.: Reconstructing the
826 Evolution of Foreland Fold-And-Thrust Belts Using U-Pb Calcite Dating: An Integrated Case-Study From the
827 Easternmost Jura Mountains (Switzerland), *Tectonics*, 43, e2023TC008181,
828 <https://doi.org/10.1029/2023TC008181>, 2024.

829 Maerten, L., Gillespie, P., and Pollard, D. D.: Effects of local stress perturbation on secondary fault development,
830 *Journal of Structural Geology*, 24, 145–153, [https://doi.org/10.1016/S0191-8141\(01\)00054-2](https://doi.org/10.1016/S0191-8141(01)00054-2), 2002.

831 Mao, J.: A finite element approach to solve contact problems in geotechnical engineering, *International Journal
832 for Numerical and Analytical Methods in Geomechanics*, 29, 525–550, <https://doi.org/10.1002/nag.424>, 2005.

833 Marchant, R., Ringgenberg, Y., Stampfli, G., Birkhäuser, P., Roth, P., and Meier, B.: Paleotectonic evolution of
834 the Zürcher Weinland (northern Switzerland), based on 2D and 3D seismic data, *Eclogae Geologicae Helvetiae*,
835 98, 345–362, <https://doi.org/10.1007/s00015-005-1171-8>, 2005.

836 McCann, T., Pascal, C., Timmerman, M. J., Krzywiec, P., López-Gómez, J., Wetzel, L., Krawczyk, C. M., Rieke,
837 H., and Lamarche, J.: Post-Variscan (end Carboniferous-Early Permian) basin evolution in Western and Central
838 Europe, *Geological Society, London, Memoirs*, 32, 355–388, <https://doi.org/10.1144/GSL.MEM.2006.032.01.22>,
839 2006.

840 Morrow, C., Radney, B., and Byerlee, J.: Chapter 3 Frictional Strength and the Effective Pressure Law of
841 Montmorillonite and Illite Clays, in: *International Geophysics*, edited by: Evans, B., and Wong, T.-f., Academic
842 Press, 69–88, [https://doi.org/10.1016/S0074-6142\(08\)62815-6](https://doi.org/10.1016/S0074-6142(08)62815-6), 1992.

843 Morrow, C., Shi, L., and Byerlee, J.: Strain hardening and strength of clay-rich fault gouges, *Journal of
844 Geophysical Research: Solid Earth*, 87, 6771–6780, <https://doi.org/10.1029/JB087iB08p06771>, 1982.

845 Nagra: Erläuterungen zur Geologischen Karte der zentralen Nordschweiz 1:100 000, NAGRA, Baden,
846 Switzerland, NAGRA Technischer Bericht NTB 84-25, 263 pp., 1984.

847 Nagra: Zur Tektonik der zentralen Nordschweiz - Interpretation aufgrund regionaler Seismik, Oberflächengeologie
848 und Tiefbohrungen, NAGRA, Wettingen, Switzerland, NAGRA Technischer Bericht NTB 90-04, 277 pp., 1991.

849 Nagra: 3D-Seismik: Räumliche Erkundung der mesozoischen Sedimentschichten im Zürcher Weinland, NAGRA,
850 Wettingen, Switzerland, NAGRA Technischer Bericht NTB 00-03, 180 pp., 2001.

851 Nagra: Geologische Entwicklung der Nordschweiz, Neotektonik und Langzeitszenarien Zürcher Weinland,
852 NAGRA, Wettingen, Switzerland, NAGRA Technischer Bericht NTB 99-08, 257 pp., 2002a.

853 Nagra: Projekt Opalinuston: Synthese der geowissenschaftlichen Untersuchungsergebnisse Entsorgungsnachweis
854 für abgebrannte Brennelemente, verglaste hochaktive sowie langlebige mittelaktive Abfälle, NAGRA, Wettingen,
855 Switzerland, NAGRA Technischer Bericht NTB 02-03, 714 pp., 2002b.

856 Nagra: Vorschlag geologischer Standortgebiete für das SMA-und das HAA-Lager, NAGRA, Wettingen,
857 Switzerland, NAGRA Technischer Bericht NTB 08-04, 477 pp., 2008.

858 Nagra: Analyse des rezenten Spannungsfelds der Nordschweiz, NAGRA, Wettingen, Switzerland, NAGRA
859 Arbeitsbericht NAB 12-05, 146 pp., 2013.

860 Nagra: Tektonische Karte des Nordschweizer Permokarbontrags: Aktualisierung basierend auf 2D-Seismik und
861 Schweredaten, NAGRA, Wettingen, Switzerland, NAGRA Arbeitsbericht NAB 14-17, 64 pp., 2014.

862 Nagra: 3D Seismic Interpretation of Stratigraphic Horizons and Structures in Time Domain, NAGRA, Wettingen,
863 Switzerland, NAGRA Arbeitsbericht NAB 23-19, 151 pp., 2024a.

864 Nagra: Geological Properties of the Jura Ost, Nördlich Lägern and Zürich Nordost Siting Regions for Safety
865 Assessment, NAGRA, Wettingen, Switzerland, NAGRA Arbeitsbericht NAB 24-10 Rev. 1, 44 pp., 2024b.

866 Nagra: Geosynthesis of Northern Switzerland, NAGRA, Wettingen, Switzerland, NAGRA Technischer Bericht
867 NTB 24-17, 604 pp., 2024c.

868 Nagra: In-Situ Stress Field in the Siting Regions Jura Ost, Nördlich Lägern and Zürich Nordost, NAGRA,
869 Wettingen, Switzerland, NAGRA Arbeitbericht NAB 24-19, 131 pp., 2024d.

870 Nicol, A., Walsh, J., Childs, C., and Manzocchi, T.: Chapter 6 - The growth of faults, in: Understanding Faults,
871 edited by: Tanner, D., and Brandes, C., Elsevier, 221–255, <https://doi.org/10.1016/B978-0-12-815985-9.00006-0>,
872 2020.

873 Pascal, C. and Gabrielsen, R. H.: Numerical modeling of Cenozoic stress patterns in the mid-Norwegian margin
874 and the northern North Sea, *Tectonics*, 20, 585–599, <https://doi.org/10.1029/2001TC900007>, 2001.

875 Pijnenburg, R. P. J., Verberne, B. A., Hangx, S. J. T., and Spiers, C. J.: Inelastic Deformation of the Slochteren
876 Sandstone: Stress-Strain Relations and Implications for Induced Seismicity in the Groningen Gas Field, *Journal*
877 *of Geophysical Research: Solid Earth*, 124, 5254–5282, <https://doi.org/10.1029/2019JB017366>, 2019.

878 Preusser, F., Graf, H. R., Keller, O., Krayss, E., and Schlüchter, C.: Quaternary glaciation history of northern
879 Switzerland, *E&G Quaternary Sci. J.*, 60, 21, <https://doi.org/10.3285/eg.60.2-3.06>, 2011.

880 Qin, X., Zhao, X., Zhang, C., Li, P., Chen, Q., and Wang, J.: Measurement and Assessment of the In-Situ Stress
881 of the Shazaoyuan Rock Block, a Candidate Site for HLW Disposal in Northwest China, *Rock Mechanics and*
882 *Rock Engineering*, 57, 4011–4031, <https://doi.org/10.1007/s00603-024-03775-z>, 2024.

883 Rajabi, M., Heidbach, O., Tingay, M., and Reiter, K.: Prediction of the present-day stress field in the Australian
884 continental crust using 3D geomechanical–numerical models, *Australian Journal of Earth Sciences*, 64, 435–454,
885 <https://doi.org/10.1080/08120099.2017.1294109>, 2017a.

886 Rajabi, M., Tingay, M., and Heidbach, O.: The present-day state of tectonic stress in the Darling Basin, Australia:
887 Implications for exploration and production, *Marine and Petroleum Geology*, 77, 776–790,
888 <https://doi.org/10.1016/j.marpetgeo.2016.07.021>, 2016.

889 Rajabi, M., Tingay, M., Heidbach, O., Hillis, R., and Reynolds, S.: The present-day stress field of Australia, *Earth-*
890 *Science Reviews*, 168, 165–189, <https://doi.org/10.1016/j.earscirev.2017.04.003>, 2017b.

891 Rajabi, M., Tingay, M., Heidbach, O., and King, R.: The Role of Faults and Fractures in Local and Regional
892 Perturbation of Present-day Horizontal Stresses - An Example from the Clarence-Moreton Basin, Eastern
893 Australia, 2015, 1–5, <https://doi.org/10.3997/2214-4609.201413346>, 2015.

894 Rajabi, M., Tingay, M., King, R., and Heidbach, O.: Present-day stress orientation in the Clarence-Moreton Basin
895 of New South Wales, Australia: a new high density dataset reveals local stress rotations, *Basin Research*, 29, 622–
896 640, <https://doi.org/10.1111/bre.12175>, 2017c.

897 Rajabi, M., Ziegler, M., Heidbach, O., Mukherjee, S., and Esterle, J.: Contribution of mine borehole data toward
898 high-resolution stress mapping: An example from northern Bowen Basin, Australia, *International Journal of Rock*
899 *Mechanics and Mining Sciences*, 173, 105630, <https://doi.org/10.1016/j.ijrmms.2023.105630>, 2024.

900 Reisdorf, A. G., Wetzel, A., Schlatter, R., and Jordan, P.: The Staffelegg Formation: a new stratigraphic scheme
901 for the Early Jurassic of northern Switzerland, *Swiss Journal of Geosciences*, 104, 97–146,
902 <https://doi.org/10.1007/s00015-011-0057-1>, 2011.

903 Reiter, K. and Heidbach, O.: 3-D geomechanical–numerical model of the contemporary crustal stress state in the
904 Alberta Basin (Canada), *Solid Earth*, 5, 1123–1149, <https://doi.org/10.5194/se-5-1123-2014>, 2014.

905 Reiter, K., Heidbach, O., and Ziegler, M. O.: Impact of faults on the remote stress state, *Solid Earth*, 15, 305–327,
906 <https://doi.org/10.5194/se-15-305-2024>, 2024.

907 Richardson, R. M., Solomon, S. C., and Sleep, N. H.: Tectonic stress in the plates, *Reviews of Geophysics*, 17,
908 981–1019, <https://doi.org/10.1029/RG017i005p00981>, 1979.

909 Roberts, D. and Myrvang, A.: Contemporary stress orientation features and horizontal stress in bedrock,
910 Trøndelag, central Norway, *NGU Bull.*, 442, 53–63, 2004.

911 Roche, V., Camanni, G., Childs, C., Manzocchi, T., Walsh, J., Conneally, J., Saqab, M. M., and Delogkos, E.:
912 Variability in the three-dimensional geometry of segmented normal fault surfaces, *Earth-Science Reviews*, 216,
913 103523, <https://doi.org/10.1016/j.earscirev.2021.103523>, 2021.

914 Saucier, F., Humphreys, E., and Weldon II, R.: Stress near geometrically complex strike-slip faults: Application
915 to the San Andreas Fault at Cajon Pass, southern California, *Journal of Geophysical Research: Solid Earth*, 97,
916 5081–5094, <https://doi.org/10.1029/91JB02644>, 1992.

917 Schmid, S. M., Pfiffner, O. A., Froitzheim, N., Schönborn, G., and Kissling, E.: Geophysical-geological transect
918 and tectonic evolution of the Swiss-Italian Alps, *Tectonics*, 15, 1036–1064, <https://doi.org/10.1029/96TC00433>,
919 1996.

920 Schmid, S. M., Pfiffner, O. A., Schönborn, G., Froitzheim, N., and Kissling, E.: Integrated cross section and
921 tectonic evolution of the Alps along the Eastern Traverse., in: *Deep Structure of the Alps, Results from NFP 20*,
922 edited by: Pfiffner, O. A., Lehner, P., Heitzmann, P., Müller, S., and Steck, A., Birkhäuser Verlag, Birkhäuser,
923 Basel, 289–304, 1997.

924 Schoenball, M., Dorbath, L., Gaucher, E., Wellmann, J. F., and Kohl, T.: Change of stress regime during
925 geothermal reservoir stimulation, *Geophysical Research Letters*, 41, 1163–1170,
926 <https://doi.org/10.1002/2013GL058514>, 2014.

927 Seithel, R., Gaucher, E., Mueller, B., Steiner, U., and Kohl, T.: Probability of fault reactivation in the Bavarian
928 Molasse Basin, *Geothermics*, 82, 81–90, <https://doi.org/10.1016/j.geothermics.2019.06.004>, 2019.

929 Sibson, R., Ghisetti, F., and Ristau, J.: Stress Control of an Evolving Strike-Slip Fault System during the 2010–
930 2011 Canterbury, New Zealand, Earthquake Sequence, *Seismological Research Letters*, 82, 824–832,
931 <https://doi.org/10.1785/gssrl.82.6.824>, 2011.

932 Sibson, R. H.: Implications of fault-valve behaviour for rupture nucleation and recurrence, *Tectonophysics*, 211,
933 283–293, [https://doi.org/10.1016/0040-1951\(92\)90065-E](https://doi.org/10.1016/0040-1951(92)90065-E), 1992.

934 Sinclair, H. D. and Allen, P. A.: Vertical versus horizontal motions in the Alpine orogenic wedge: stratigraphic
935 response in the foreland basin, *Basin Research*, 4, 215–232, <https://doi.org/10.1111/j.1365-2117.1992.tb00046.x>,
936 1992.

937 Smart, K. J., Ferrill, D. A., Morris, A. P., and McGinnis, R. N.: Geomechanical modeling of stress and strain
938 evolution during contractional fault-related folding, *Tectonophysics*, 576–577, 171–196,
939 <https://doi.org/10.1016/j.tecto.2012.05.024>, 2012.

940 Sommaruga, A., Eichenberger, U., and Marillier, F.: Seismic Atlas of the Swiss Molasse Basin, *Matériaux pour la
941 Géologie de la Suisse – Géophysique*, 2012.

942 Stromeyer, D., Heidbach, O., and Ziegler, M.: Tecplot 360 Add-on GeoStress v. 2.0. V. 2.0, GFZ Data Services
943 [code], <https://doi.org/10.5880/wsm.2020.001>, 2020.

944 Su, S. and Stephansson, O.: Effect of a fault on in situ stresses studied by the distinct element method, International
945 Journal of Rock Mechanics and Mining Sciences, 36, 1051–1056, [https://doi.org/10.1016/S1365-1609\(99\)00119-2](https://doi.org/10.1016/S1365-1609(99)00119-2), 1999.

947 Tanner, D. C. and Brandes, C.: Chapter 1 - Introduction, in: Understanding Faults, edited by: Tanner, D., and
948 Brandes, C., Elsevier, 1–10, <https://doi.org/10.1016/B978-0-12-815985-9.00001-1>, 2020.

949 Tavener, E., Flottmann, T., and Brooke-Barnett, S.: In situ stress distribution and mechanical stratigraphy in the
950 Bowen and Surat basins, Queensland, Australia, Geological Society, London, Special Publications, 458, 31–47,
951 doi:10.1144/SP458.4, 2017.

952 Tingay, M. R. P., Hillis, R. R., Morley, C. K., King, R. C., Swarbrick, R. E., and Damit, A. R.: Present-day stress
953 and neotectonics of Brunei: Implications for petroleum exploration and production, AAPG Bulletin, 93, 75–100,
954 <https://doi.org/10.1306/08080808031>, 2009.

955 Treffeisen, T. and Henk, A.: Representation of faults in reservoir-scale geomechanical finite element models – A
956 comparison of different modelling approaches, Journal of Structural Geology, 131, 103931,
957 <https://doi.org/10.1016/j.jsg.2019.103931>, 2020.

958 Vadacca, L., Rossi, D., Scotti, A., and Buttinelli, M.: Slip Tendency Analysis, Fault Reactivation Potential and
959 Induced Seismicity in the Val d'Agri Oilfield (Italy), Journal of Geophysical Research: Solid Earth, 126,
960 2019JB019185, <https://doi.org/10.1029/2019JB019185>, 2021.

961 Viganò, A., Ranalli, G., Andreis, D., and Martin, S.: Inversion for the static friction coefficient of seismogenic
962 faults: Application to induced seismicity of the Basel Enhanced Geothermal System, Switzerland, Journal of
963 Geodynamics, 145, 101843, <https://doi.org/10.1016/j.jog.2021.101843>, 2021.

964 Yale, D. P.: Fault and stress magnitude controls on variations in the orientation of in situ stress, in: Fracture and
965 In-Situ Stress Characterization of Hydrocarbon Reservoirs, edited by: Ameen, M., Geological Society of London,
966 0, <https://doi.org/10.1144/GSL.SP.2003.209.01.06>, 2003.

967 Yale, D. P., Rodriguez, J. M., Mercer, T. B., and Blaisdell, D. W.: In-situ Stress Orientation and the Effects of
968 Local Structure – Scott Field, North Sea, Rock Mechanics in Petroleum Engineering, Delft, Netherlands, 29–31
969 Aug, <https://doi.org/10.2118/28146-MS>, 1994.

970 Yale, D. P. and Ryan, T. C.: In-Situ Stress and Hydraulic Fracture Orientation in the Mid-Continent Area, US, 1st
971 North American Rock Mechanics Symposium, Austin, Texas, 1–3 June, 1994.

972 Yale, D. P., Strubhar, M. K., and El Rabaa, A. W.: Determination of Hydraulic Fracture Direction, San Juan Basin,
973 New Mexico, SPE Production Operations Symposium, Oklahoma City, Oklahoma 21–23 March,
974 <https://doi.org/10.2118/25466-MS>, 1993.

975 Yan, H., Bakk, A., Holt, R. M., and Lozovskyi, S.: Numerical analysis of stress path evolution in the overburden of
976 depleting reservoirs: a parametric study, Geomechanics and Geophysics for Geo-Energy and Geo-Resources, 11,
977 91, 10.1007/s40948-025-00989-5, 2025.

978 Zakhrova, N. V. and Goldberg, D. S.: In situ stress analysis in the northern Newark Basin: Implications for
979 induced seismicity from CO₂ injection, Journal of Geophysical Research: Solid Earth, 119, 2362–2374,
980 <https://doi.org/10.1002/2013JB010492>, 2014.

981 Zang, A. and Stephansson, O.: Stress field of the earth's crust, 2010, Springer Dordrecht, New York, NY, 324 pp.,
982 <https://doi.org/10.1007/978-1-4020-8444-7>, 2010.

983 Ziegler, M. O. and Heidbach, O.: The 3D stress state from geomechanical-numerical modelling and its
984 uncertainties: a case study in the Bavarian Molasse Basin, Geothermal Energy, 8, 11,
985 <https://doi.org/10.1186/s40517-020-00162-z>, 2020.

986 Ziegler, M. O. and Heidbach, O.: Python Script PyFAST Calibration v.1.0 V. 1.0, GFZ Data Services [code],
987 <https://doi.org/10.5880/wsm.2021.003>, 2021.

988 Ziegler, M. O., Heidbach, O., Reinecker, J., Przybycin, A. M., and Scheck-Wenderoth, M.: A multi-stage 3-D
989 stress field modelling approach exemplified in the Bavarian Molasse Basin, *Solid Earth*, 7, 1365–1382,
990 <https://doi.org/10.5194/se-7-1365-2016>, 2016.

991 Ziegler, M. O., Seithel, R., Niederhuber, T., Heidbach, O., Kohl, T., Müller, B., Rajabi, M., Reiter, K., and Röckel,
992 L.: Stress state at faults: the influence of rock stiffness contrast, stress orientation, and ratio, *Solid Earth*, 15, 1047–
993 1063, <https://doi.org/10.5194/se-15-1047-2024>, 2024.

994 Ziegler, M. O., Ziebarth, M., and Reiter, K.: Python Script Apple PY v1.3. V. 1.3,
995 <https://doi.org/10.5880/wsm.2020.002>, 2020.

996 Zoback, M. and Healy, J.: Friction, faulting and in situ stress, *Annales geophysicae* (1983), 2, 689–698, 1984.

997 Zoback, M., Hickman, S., Ellsworth, W., and the, S. S. T.: Scientific Drilling Into the San Andreas Fault Zone -
998 An Overview of SAFOD's First Five Years, *Sci. Dril.*, 11, 14–28, <https://doi.org/10.2204/iodp.sd.11.02.2011>,
999 2011.

1000 Zoback, M. D.: *Reservoir Geomechanics*, Cambridge University Press, Cambridge,
1001 <https://doi.org/10.1017/CBO9780511586477>, 2009.

1002 Zoback, M. D., Zoback, M. L., Mount, V. S., Suppe, J., Eaton, J. P., Healy, J. H., Oppenheimer, D., Reasenberg,
1003 P., Jones, L., Raleigh, C. B., Wong, I. G., Scotti, O., and Wentworth, C.: New Evidence on the State of Stress of
1004 the San Andreas Fault System, *Science*, 238, 1105–1111, <https://doi.org/10.1126/science.238.4830.1105>, 1987.

1005 Zoback, M. L.: First- and second-order patterns of stress in the lithosphere: The World Stress Map Project, *Journal*
1006 *of Geophysical Research: Solid Earth*, 97, 11703–11728, <https://doi.org/10.1029/92JB00132>, 1992.

1007 Zoback, M. L., Zoback, M. D., Adams, J., Assumpção, M., Bell, S., Bergman, E. A., Blümling, P., Brereton, N.
1008 R., Denham, D., Ding, J., Fuchs, K., Gay, N., Gregersen, S., Gupta, H. K., Gvishiani, A., Jacob, K., Klein, R.,
1009 Knoll, P., Magee, M., Mercier, J. L., Müller, B. C., Paquin, C., Rajendran, K., Stephansson, O., Suarez, G., Suter,
1010 M., Udiás, A., Xu, Z. H., and Zhizhin, M.: Global patterns of tectonic stress, *Nature*, 341, 291–298,
1011 <https://doi.org/10.1038/341291a0>, 1989.

1012